

# Isomerization and Decomposition Reactions of Acetaldehyde Relevant to Atmospheric Processes from Dynamics Simulations on Neural Network-Based Potential Energy Surfaces

Silvan Käser,<sup>†</sup> Oliver T. Unke,<sup>‡</sup> and Markus Meuwly<sup>\*,†</sup>

<sup>†</sup>*Department of Chemistry, University of Basel, Klingelbergstrasse 80, CH-4056 Basel,  
Switzerland.*

<sup>‡</sup>*Department of Chemistry, University of Basel, Klingelbergstrasse 80, CH-4056 Basel,  
Switzerland*

*Present Address: Machine Learning Group, TU Berlin, Marchstr. 23, 10587 Berlin,  
Germany*

E-mail: m.meuwly@unibas.ch

## Abstract

Acetaldehyde (AA) isomerization (to vinylalcohol, VA) and decomposition (into either  $\text{CO}+\text{CH}_4$  and  $\text{H}_2+\text{H}_2\text{CCO}$ ) is studied using a fully dimensional, reactive potential energy surface represented as a neural network (NN). The NN, trained on 432'399 reference structures from MP2/aug-cc-pVTZ calculations has a MAE of 0.0453 kcal/mol and an RMSE of 1.186 kcal/mol for a test set of 27'399 structures. For the isomerization process  $\text{AA}\rightarrow\text{VA}$  the minimum dynamical path implies that the CH vibration, and the CCH (with H being the transferring H-atom) and the CCO angles are involved to surmount the 68.2 kcal/mol barrier. Using an excess energy of 93.6 kcal/mol – the energy available in the solar spectrum and sufficient to excite to the first electronically excited state – to initialize the molecular dynamics, no isomerization to VA is observed on the 500 ns time scale. Only with excess energies of  $\sim 127.6$  kcal/mol (including the zero point energy of the AA molecule), isomerization occurs on the nanosecond time scale. Given that collisional de-excitation at atmospheric conditions in the stratosphere occurs on the 100 ns time scale, it is concluded that formation of VA following photoexcitation of AA from actinic photons is unlikely. This also limits the relevance of this reaction pathway to be a source for formic acid.

## 1 Introduction

Understanding and quantifying the relative importance of tautomerization versus decomposition reactions of small organic molecules is an essential aspect in modeling atmospheric processes.<sup>1</sup> Recently, the photo-tautomerization of acetaldehyde (AA) to vinyl alcohol (VA) has been investigated experimentally<sup>2</sup> and the results were linked to formic acid (FA) production in the atmosphere.<sup>2,3</sup> Although the experiments provided insight into the tautomerization dynamics, the time scale on which the  $\text{AA}\rightarrow\text{VA}$  isomerization occurs is still unknown.

In general, the role of photo-induced tautomerization of carbonyls in atmospheric modeling is incompletely characterized.<sup>4,5</sup> In such systems, interconversion barrier heights for tautomerization and fragmentation can be similar which leads to competing reaction pathways. This situation is similar to halogenated sulfur-containing compounds (such as  $\text{H}_2\text{SO}_4$  or  $\text{HSO}_3\text{F}$ ) for which proton transfer barrier heights (isomerization) only differ by a few kcal/mol compared with those leading to  $\text{SO}_3 + \text{H}_2\text{O}$  (for  $\text{H}_2\text{SO}_4$ ) or  $\text{HF} + \text{H}_2\text{O}$  (for  $\text{HSO}_3\text{F}$ ),<sup>6-9</sup> important processes that have also been implicated in atmospheric chemistry.<sup>10</sup> Such a topography of the potential energy surface (PES) leads to rich molecular dynamics and a broad distribution of reaction times for the fragmentation process due to internal vibrational energy redistribution (IVR).

For a molecularly refined understanding of the reaction dynamics and for determining the corresponding rates, accurate and fully-dimensional PESs for reactive atomistic simulations are required. An essential prerequisite for molecular dynamics (MD) simulations is the availability of energies and corresponding forces for an extensive range of molecular configurations, which can either be obtained from solving the electronic Schrödinger equation at every time step of an MD simulation (QM/MD or *ab initio* MD) or by parametrizing a suitable reactive force field such as in multi state adiabatic reactive MD.<sup>7</sup>

Due to the unfavourable scaling of high-accuracy electronic structure methods with the number of electrons (and basis functions required for an accurate description) it is only possible to use *ab initio* MD methods for small molecules in the gas phase and for short time scales (several 10 picoseconds).<sup>11</sup> These limitations often make examining interesting chemical or physical problems difficult. To overcome this it is necessary to find computationally efficient representations of the intermolecular interactions to describe the energies of molecular configurations. One such approach are reactive MD simulations<sup>12,13</sup> which allow to study the breaking and formation of chemical bonds.

More recently, artificial neural networks (ANNs) have emerged as an alternative way to fit and calculate the energies of molecules based on a large number of reference electronic structure calculations. NNs were introduced more than half a century ago<sup>14,15</sup> and are a set of biology-inspired algorithms which learn patterns and interrelations from extensive data.<sup>16,17</sup> Because they are general function approximators<sup>18</sup> they constitute an ideal tool for generating representations of molecular PESs.

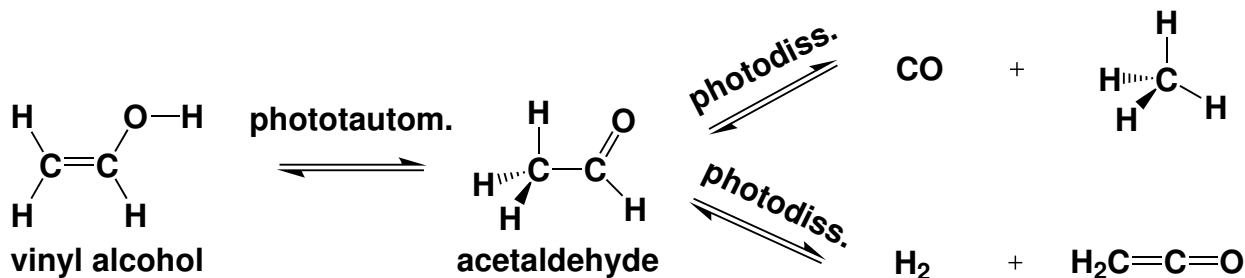


Figure 1: Schematic molecular representation of the tautomerization and dissociations of acetaldehyde (AA, middle). Here, isomerization to vinylalcohol (VA, left) and dissociation to  $\text{CO}+\text{CH}_4$  and  $\text{H}_2+\text{C}_2\text{OH}_2$  (right) is studied

In the present work a reactive, global NN-based PES is developed for acetaldehyde (AA) to study tautomerization and decomposition reactions. AA ( $\text{CH}_3\text{CHO}$ ) plays an important role in atmospheric chemistry by adversely affecting global climate.<sup>19</sup> The smallest organic acids – FA and acetic acid – make up a significant fraction of the tropospheric organic acids. The majority of atmospheric organic acids are believed to be generated via photochemical oxidation of biogenic and anthropogenic volatile organic compounds (VOCs). However, the global budget for FA indicates that in addition to the largest source for FA (e.g. photochemical production through fires, oxidation of organic aerosols) other formation pathways must contribute.<sup>20</sup> One proposed formation pathway is the generation of FA via oxidation by the hydroxyl radical<sup>2,21</sup> following photo-tautomerization of AA to its enol form VA.<sup>3-5</sup> The relevant states for tautomerization of AA to VA, the dissociation to carbon monoxide and methane, and the dissociation to  $\text{H}_2$  and ketene are shown in Figure 1.

Recent laboratory experiments under atmospheric conditions reported direct evidence that AA does photo-tautomerize to VA. To this end, pressure- and wavelength-dependent quantum yields for VA production in up to 1 atm of N<sub>2</sub> in the actinic wavelength range of  $\lambda = 300$  to 330 nm (corresponding to an excitation energy of  $\sim 95$  kcal/mol) were determined.<sup>2</sup> One of the pertinent questions is therefore whether isomerization from an electronically excited AA to VA competes kinetically with collisional de-excitation through other molecules in the atmosphere and other competing intramolecular pathways such as decomposition into CO and CH<sub>4</sub> or into H<sub>2</sub> and H<sub>2</sub>CCO. For this, typical isomerization times are required which have so far not been obtained from experiment but can be determined from reactive MD simulations. To carry out such simulations, a reliable, fully dimensional reactive PES is required in order to follow the nonequilibrium dynamics after electronic excitation and relaxation of AA into relevant states – including VA, CH<sub>4</sub>+CO, and H<sub>2</sub>+H<sub>2</sub>CCO, see Figure 1.

Previous computational studies using QCT simulations focused on the final state analysis<sup>22</sup> and branching ratio<sup>23</sup> at high energies for several reaction products. The simulations were based on a PES fitted to permutationally invariant polynomials.<sup>24</sup> Other related processes that were recently studied included formic acid-assisted conversion of VA to AA<sup>25</sup> and the oxidation of VA by the hydroxyl radical (OH) which was found to be fast and generates mainly FA.<sup>21</sup>

In the present work a neural network-based PES is employed to carry out reactive molecular dynamics simulations for a large number of diverse initial conditions. In the following, first the construction of the NN PES is described. Then, the minimum dynamical path (MDP)<sup>26</sup> connecting different states is determined and reactive MDs are run and analyzed. Finally, the results are discussed in the context of atmospheric chemistry.

## 2 Methods

First, the development of the NN-based, reactive PES for AA and its isomerization (VA) and several reaction products ( $\text{CH}_4+\text{CO}$ ,  $\text{H}_2+\text{H}_2\text{CCO}$ ) is described. This includes the generation of reference data, as well as the architecture and training of the NN. Section 2.2 outlines the protocol used for the molecular dynamics (MD) simulations and their analysis. All programs used for the reference data set and MD simulations were written in the Python programming language and used the Atomic Simulation Environment (ASE).<sup>27</sup>

### 2.1 Construction of the Potential Energy Surface

The present work uses PhysNet,<sup>28</sup> a high-dimensional NN<sup>29</sup> designed to learn molecular properties including energy, forces, and dipole moments from *ab initio* reference data, to construct the PES. In the following, its architecture and the generation of reference data are briefly summarized. For more details the reader is referred to Reference 28.

PhysNet predicts atomic energy contributions and partial charges based on feature vectors that encode the local chemical environment<sup>30</sup> of each atom  $i$ . These features are constructed by “passing messages”<sup>31</sup> between all atoms within a cutoff radius of  $r_{\text{cut}} = 10 \text{ \AA}$  and encode information about nuclear charges  $Z_i$  and Cartesian coordinates  $\mathbf{r}_i$ . The total potential energy  $E$  of the system is the sum of all  $N$  atomic contributions and includes long-range electrostatics and dispersion interactions explicitly:

$$E = \sum_{i=1}^N E_i + k_e \sum_{i=1}^N \sum_{j>i}^N \frac{q_i q_j}{r_{ij}} + E_{\text{D3}} \quad (1)$$

Here,  $E_i$  and  $q_i$  are atomic energy contributions and partial charges (corrected to guarantee charge conservation, see Reference 28),  $k_e$  is Coulomb’s constant,  $r_{ij}$  is the distance between atoms  $i$  and  $j$  and  $E_{\text{D3}}$  is Grimme’s D3 dispersion correction.<sup>32</sup> To prevent potential numer-

ical instabilities due to the singularity at  $r_{ij} = 0$ , the Coulomb term is damped for small distances (see Reference 28, not shown in Eq. 1). The parameters for the dispersion correction, which are adapted during the training procedure, are initialized to the standard values recommended for the Hartree-Fock level of theory.<sup>33</sup> Since the atomic features (from which  $E_i$  and  $q_i$  are derived) are constructed based only on pairwise distances, and the influence of all atoms within the cutoff is combined by summation, the energy  $E$  is invariant with respect to translation, rotation, as well as permutations of equivalent atoms. Analytical derivatives of  $E$  with respect to the Cartesian coordinates  $\mathbf{r}_i$ , required for the forces in the MD simulations, are obtained by reverse mode automatic differentiation.<sup>34</sup>

In order to construct a PES, *ab initio* reference data is required for training the NN. Here, the MP2/aug-cc-pVTZ level of theory<sup>35,36</sup> is used as a compromise between speed and accuracy. Although single point calculations would also be possible at a higher level of theory, such as CCSD(T),<sup>22</sup> a lower level is preferred here because the number of reference calculations required to reliably represent a high-dimensional, reactive PES is unknown *a priori*. As is described further below, the final data set required to run stable MD simulations contains more than 400'000 energies for the present work which would be computationally very demanding to be determined at a higher level. The reference data (energies, forces and dipole moments) are calculated using the MOLPRO software package.<sup>37</sup>

Motivated by the “amons” approach,<sup>38</sup> a set of molecules covering a range of fragmentation products and stable intermediates is chosen (see Figure S1). Then, MD simulations for all these molecules and the van der Waals complexes of the fragmentation products  $\text{CH}_4 + \text{CO}$  and  $\text{H}_2 + \text{H}_2\text{CCO}$  are run to obtain a broad range of molecular geometries. All simulations start at the optimized geometries and are propagated using Langevin dynamics at 1000 K using a time step of 0.1 fs. The forces are obtained at the semi-empirical PM7<sup>39</sup> level of theory using MOPAC.<sup>40</sup> For the van der Waals complexes, complete dissociation is prevented

using a harmonic potential, akin to umbrella sampling.<sup>41</sup> In the same way, structures around the transition states (TSs) are sampled by harmonically biasing the geometry towards the TS structure.

On this initial data set, two independent NNs are trained and the MD simulations are repeated using their averaged predictions to obtain the necessary forces. Then, the data set is extended based on adaptive sampling:<sup>42,43</sup> If the energy predictions of both NNs differ by more than a threshold value (here 0.5 kcal/mol) during the simulations, this indicates that the reference data is insufficient to describe this part of the PES. The corresponding structures are saved and new *ab initio* calculations are performed and added to the data set. Then, the NNs are re-trained on the extended data set and the sampling is repeated until differences (0.5 kcal/mol, see above) between the NN predictions are either rare or nonexistent. After the third iteration, the dataset is cleaned by removing outliers from the ensemble of networks for which  $|E_{\text{MP2}} - E_{\text{NN}}| > 3$  kcal/mol. Such structures with large prediction errors are typically generated at an early stage of the adaptive sampling when the global PES is still insufficiently sampled. The last two iterations of structure sampling were performed based on the normal mode sampling method.<sup>44</sup>

After a total of six iterations, the final data set contained 432'399 structures. The data set was then split into a training (380'000), a validation (25'000), and a test set (27'399) and used to train the final NNs. The subsequent analysis and MD simulations are performed using one NN, unless stated otherwise.

## 2.2 Molecular Dynamics Simulations

The final NN PES was first used to examine the minimum dynamical path (MDP) and to run different types of MD simulations starting from a range of initial conditions. The MDP



corresponds to the path a trajectory follows when going from a reactant to a product (or vice versa) and passing through the exact transition state with zero excess energy.<sup>26</sup> It can be calculated by assigning infinitesimal momenta along the normal mode vector with imaginary frequency and then advancing the MD simulation from a TS. The MDP is examined in order to characterize the internal degrees of freedom that are dynamically coupled when transitioning from reactant to product. For example, by analysing the MDP for a Diels-Alder reaction, it was found - and subsequently confirmed from explicit MD simulations - that relative rotational motion of the reactants promotes product formation.<sup>45</sup> Such insights are difficult to obtain from a static picture of a reactive process, e.g. via the minimum energy path (MEP).

All simulations were carried out in the microcanonical ( $NVE$ ) ensemble using the Velocity Verlet integrator<sup>46</sup> with a time step of  $\Delta t = 0.1$  fs. The first set of MD simulations is started from the optimized AA structure. Random momenta are assigned and scaled such that the total kinetic energy is  $E_{\text{ex}} = 93.6$  kcal/mol. This energy corresponds to the total energy content of the molecule after returning to the ground state PES following photoexcitation and is slightly lower than the maximum excitation energy used in the experiments which is  $\sim 95$  kcal/mol.<sup>2</sup> 2000 trajectories with different initial momenta are run for 250 ps each, yielding a total of 500 ns simulation time. In the following, this set of simulations is referred to as *EX* (excitation) trajectories.

For the second set of simulations, the energy of the system was increased to 127.6 kcal/mol, as was done in Reference 47. This energy includes the excitation energy  $E_{\text{ex}}$  and the harmonic zero point energy (ZPE) of AA. The ZPE of AA was also calculated for the NN PES (35.1 kcal/mol) and found to be within 0.3 kcal/mol of the energy used in Reference 47 (34.8 kcal/mol at the CCSD(T) level of theory). A total of 10'000 trajectories, each 50 ps in length, are run, yielding a total simulation time of 500 ns. This set of trajectories will be

referred to as *ZPE*.

Because the MD simulations are run at large excess energy on the ground state PES, the validity of the NN for the structures sampled needs to be checked thoroughly. For this, all trajectories are analyzed for unusual molecular structures – such as unusually short atom-atom separations or dissociations – based on geometric considerations. Moreover, the energy of single trajectories is evaluated with two independently trained NNs and their energy prediction is compared (see Figure S2).

### 3 Results

First, the accuracy of the NN-PES is investigated. Next, the minimum dynamical paths (MDPs)<sup>26</sup> along the reaction pathways for the tautomerization between AA and VA, the dissociation to methane and carbon monoxide, and the dissociation to H<sub>2</sub> and ketene (see Figure 1) are explored in order to characterize the internal degrees of freedom that are involved in the different atomic rearrangements. Finally, the two sets of trajectories are analyzed and the likelihood for reaction is assessed.

#### 3.1 Quality of the Potential Energy Surface

The accuracy of the NN PES is examined by comparing the predicted NN energies with the reference MP2 energies for the 27’399 test set structures, see Figure 2. Most of the NN energies match the MP2 energies, except for a few outliers. The MAE is 0.0453 kcal/mol with an RMSE of 1.186 kcal/mol and a Pearson coefficient of  $1 - 2.86 \cdot 10^{-5}$  when compared with the reference calculations. Three outliers (below the red line) with unusually large CH (up to 2.65 Å), CO (up to 2.34 Å), and CC (up to 2.72 Å) separations are present in the

test set. These were sampled in the early adaptive sampling runs.

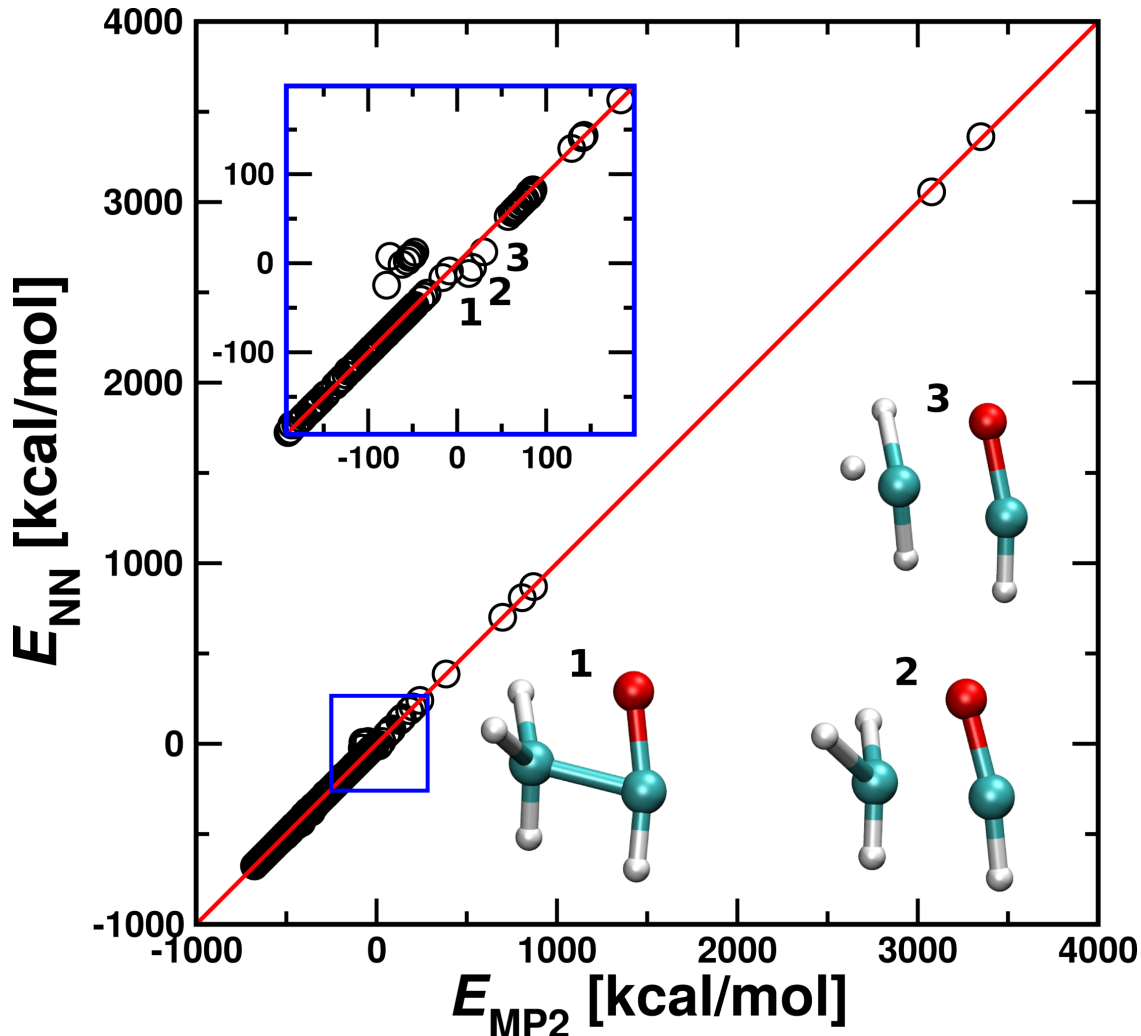


Figure 2: Comparison of the MP2 reference and predicted NN energies for the test set. The 27399 structures from the test set are predicted with a MAE of 0.0453 kcal/mol, an RMSE of 1.186 kcal/mol and a Pearson coefficient of  $1 - 2.86 \cdot 10^{-5}$ . The graph is complemented with a zoom-in (blue) and three outlier structures (1 to 3) and nine outliers above the diagonal. All outliers including their  $T_1$  value<sup>48</sup> are reported in Figure S3. For structures in the insets, “bonds” are shown up to a distance of 2.6 Å.

Moreover, the enlargement reveals a group of nine structures with a comparable error of  $\approx 60$  kcal/mol (above red line). Sampling structures far from equilibrium for the molecules considered potentially leads into regions of the PES where multireference effects can become relevant. To test this, the  $T_1$  diagnostic<sup>48</sup> is determined for these outliers which are charac-

terized by unusual geometries with elongated bonds (see Figure S3). A value for  $T_1 > 0.02$  indicates that a single-reference wavefunction may be insufficient to describe the system. The  $T_1$  values were calculated at the (pair natural orbital - local CCSD(T)) PNO-LCCSD(T)-F12/cc-pVTZ-F12 level of theory.<sup>49</sup> For most structures, the  $T_1$  diagnostic is well above a value of 0.02 (Figure S3). Hence, their multireference character may be the reason for the large prediction errors. It has already been shown earlier that NNs can be effective to identify members in a test set that are likely outliers.<sup>30</sup>

The energies of the tautomerization and dissociation products from using the NN (referenced to the optimized structure of AA) are summarized in Figure 3. Tautomerization to VA, which is 10.1 kcal/mol higher in energy than AA, involves an activation energy of  $\sim 68$  kcal/mol. The two dissociation reactions have a similar barrier height (to within  $\sim 4$  kcal/mol). Table 1 confirms that the NN performs well and captures the reference MP2 calculations to within 0.2 kcal/mol. For comparison, energies are also reported from CCSD(T) calculations which are within 1.0 kcal/mol of the MP2 values except for the  $\text{CH}_4 + \text{CO}$  dissociation channel which is less relevant for the present work.

**Table 1: Comparison of the MP2/aug-cc-pVTZ reference and NN-predicted energies for the processes considered. Differences are  $\leq 0.2$  kcal/mol. For completeness the energies are compared to CCSD(T) energies from Reference 2. The zero of energy is the optimized structure of AA.**

[kcal/mol]	VA	TS1	AA	TS2	$\text{CH}_4 + \text{CO}$	TS3	ketene + $\text{H}_2$
$E_{\text{NN}}$	10.1	68.1	0	88.2	-2.2	84.2	33.8
$E_{\text{MP2}}$	10.1	68.1	0	88.2	-2.2	84.2	34.0
$E_{\text{CCSD(T)}}$	10.6	67.7	0	83.3	-6.0	-	-

### 3.2 Minimum Dynamical Path

Structures along the MDPs for the three processes considered here are shown in Figures 4 to 6. The TS is marked with a red border and connects reactant (AA) and product (VA,

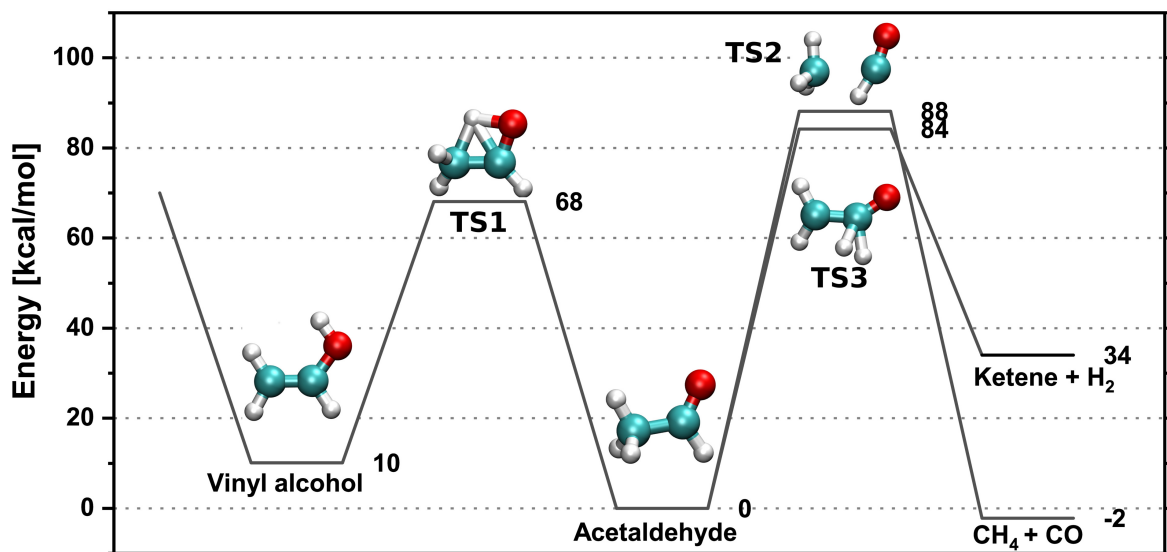


Figure 3: Schematic representation of the PES predicted by the NN based on MP2/aug-cc-pVTZ reference calculations for the three reactions: the tautomerization (to the left) and the two dissociation reactions (to the right). All energies are referenced to that of AA. The optimized structures and the transition states are illustrated, and the corresponding energies are displayed.

CH<sub>4</sub>+CO, or OC<sub>2</sub>H<sub>2</sub>+H<sub>2</sub>) states from left to right. For the tautomerization reaction (Figure 4) the transferring H-atom is involved in a highly excited C-H vibration (see Figure S4, green line for  $t < 0$ ) with large amplitude motion along the CCH angle (Figure S4, red line for  $t < 0$ ) which is also coupled to the OH distance fluctuation before reaching the TS (Figure S4, blue line for  $t < 0$ ). Shortly before the TS the H-atoms not involved in hydrogen transfer (HT) rotate slightly (see Figure 4) which reduces both, the CCH and the CCO angles. After HT the O-H bond is highly vibrationally excited (Figure S4, blue line for  $t > 0$ ) and coupled with an out-of-plane rotation of the O-H bond (last 3 snapshots of Figure 4). Moreover, upon hydrogen transfer the CCH and CCO bending vibrations are out-of-phase by  $\pi$ .

For the CH<sub>4</sub>+ CO dissociation the MDP involves a large-amplitude CH vibration (Figure S5, blue line  $t < 0$ ) and a pronounced oscillation of the OCH bend (between 75° and 170°, Fig-

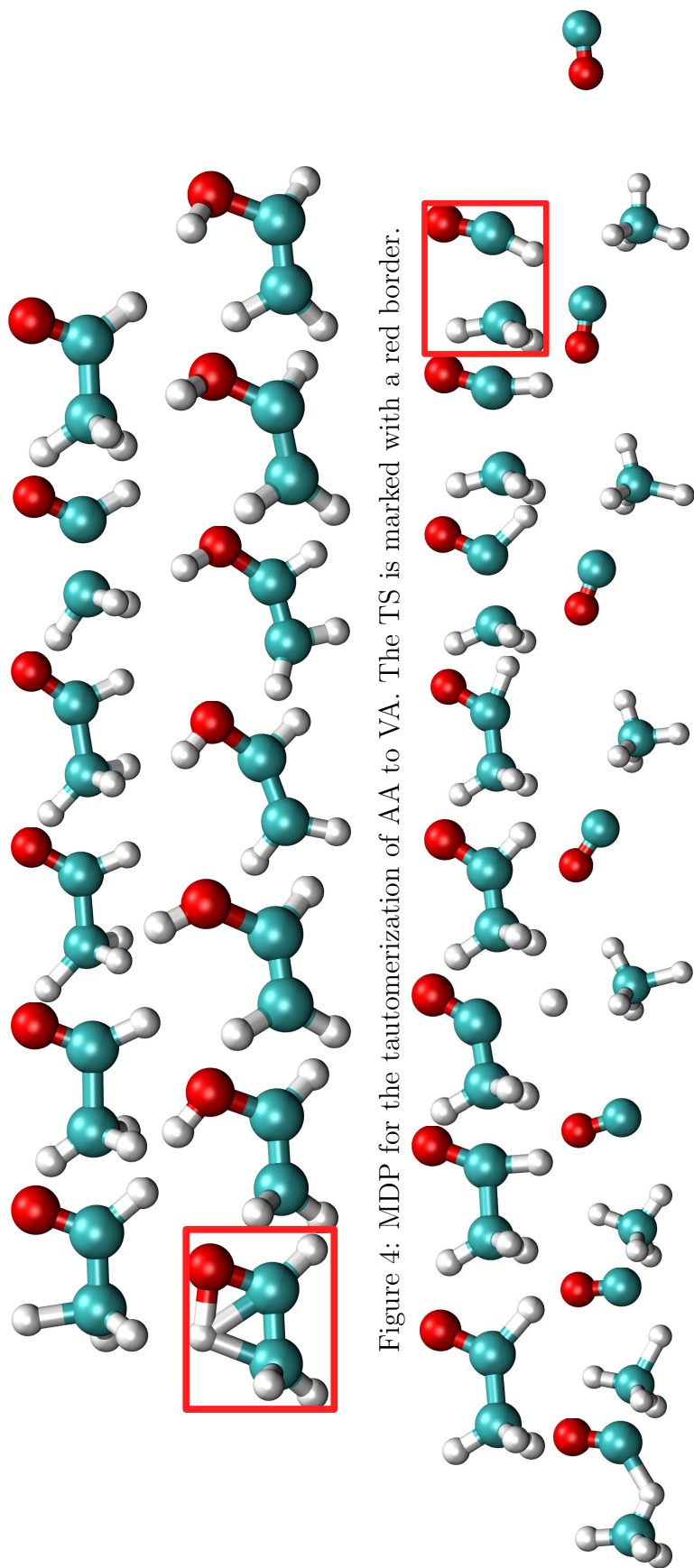


Figure 4: MDP for the tautomerization of AA to VA. The TS is marked with a red border.

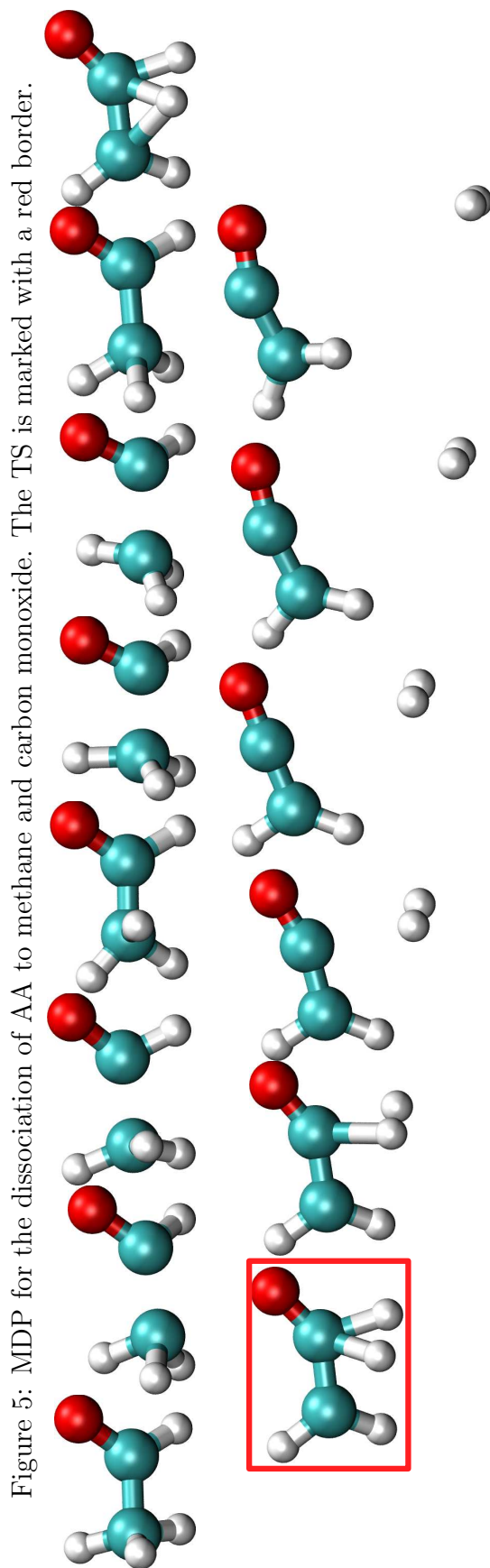


Figure 5: MDP for the dissociation of AA to methane and carbon monoxide. The TS is marked with a red border.

Figure 6: MDP for the dissociation of AA to  $H_2$  and ketene. The TS is marked with a red border.

ure S5, black line) while the methyl rotation is locked, see Figure 5. For the HT from the COH moiety to the CH<sub>3</sub> group to occur, the CC bond needs to stretch and be accompanied by OCH bending (peak in OCH angle, see Figure S5). Upon dissociation ( $t > 0$ ) the transferred H-atom exhibits a highly excited CH (Figure S5, green line) vibration and the dissociation products are rotationally excited due to the anisotropy of the potential energy surface.

For the dissociation to H<sub>2</sub>+H<sub>2</sub>CCO the MDP (see Figure 6) shows that the CC and CH bonds involving the dissociating H-atoms, which eventually combine to form H<sub>2</sub>, are highly vibrationally excited. Moreover, an umbrella motion of the hydrogen (strong oscillation of the CCH angle between 75° and 150° (Figure S6, black line) facilitates the approach of the two H-atoms. After crossing the TS the H<sub>2</sub> gains rotational as well as translational energy whereas the kinetic energy of the ketene is visible in a bending of the CCO angle (Figure S6, red line).

For completeness, structures along the minimum energy path (MEP) are also reported in Figures S7 to S9. Compared to the MDP, the MEP lacks important dynamic information. For example, the oscillation of the CCO angle in the tautomerization does not appear in the MEP but plays an essential role in the MDP.

### 3.3 Molecular Dynamics Simulations

First, the trajectories run at conditions representative for electronic excitation by solar photons and recent experiments<sup>2</sup> (*EX* trajectories) are analyzed. Here, the excitation energy is 93.6 kcal/mol which compares with energies of 86.6 kcal/mol to 95.3 kcal/mol for actinic photons. All *EX* trajectories starting from the optimized AA structure remained in the AA well and none of the 2000 trajectories exhibited isomerization to VA. In other words, starting

from the structure after photoexcitation, IVR is very efficient and localizes the system in the AA structure. Although the energized AA contains sufficient energy to isomerize to VA ( $\sim 94$  kcal/mol compared with a barrier height of 68 kcal/mol for isomerization to VA), no such process is found after a total simulation time of 500 ns. This suggests that on the  $\sim 100$  ns time scale isomerization AA $\rightarrow$ VA is unlikely for excitation energies compatible with actinic photons.

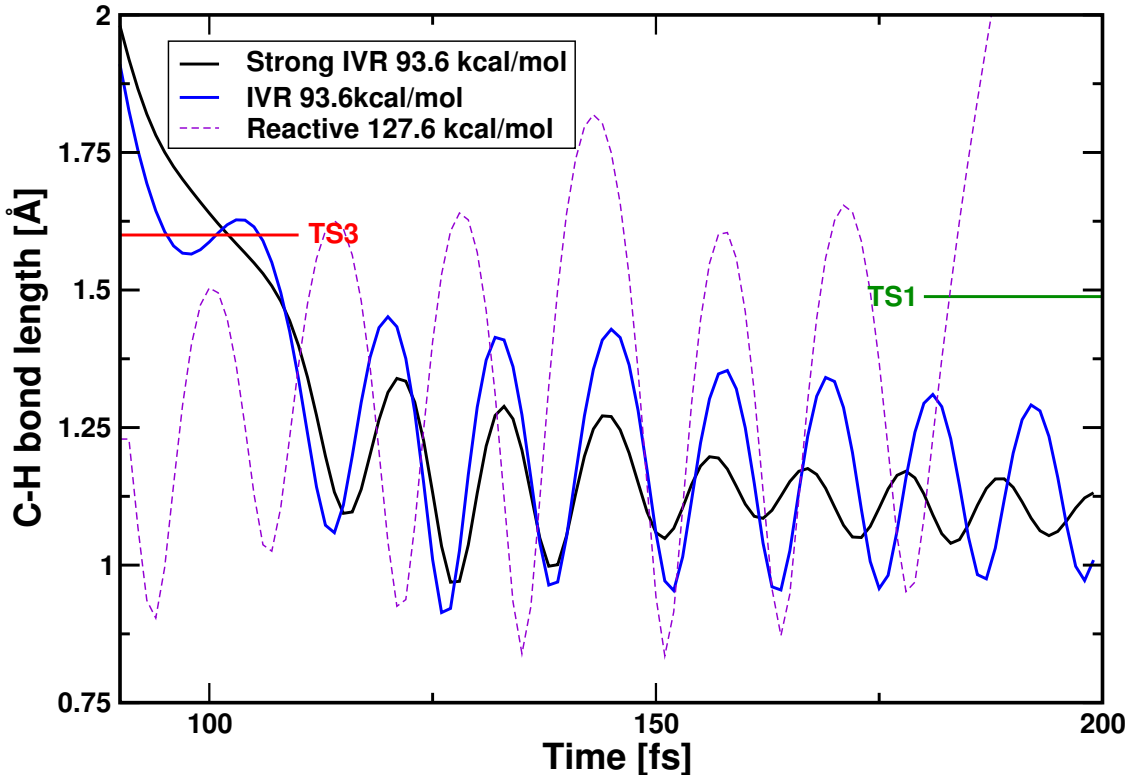


Figure 7: The time series for the CH stretch for three different trajectories. Two trajectories are started from TS3 with an energy of 93.6 kcal/mol with respect to the ground state AA (blue and black). For the black trace the motion along the CH mode is strongly damped. The red line indicates the CH bond length of TS3 and the green line corresponds to TS1 connecting AA and VA (see Figure 3) which needs to be reached for AA $\rightarrow$ VA isomerization. The purple line corresponds to the CH stretch of a reactive ZPE trajectory undergoing AA $\rightarrow$ VA reaction.

To further investigate the role of IVR, five independent trajectories were started from TS3 with an excess energy of 93.6 kcal/mol with respect to the ground state of AA. The analysis



of these trajectories relaxing from TS3 towards AA reveals that the energy is rapidly (few tens of fs) distributed among the different modes (see Figure 7). In order to validate these findings, separate *ab initio* MD simulations were run using the semiempirical tight binding GFN2-xTB<sup>50</sup> method. These simulations support that IVR of the relevant CH stretch modes occur on the sub-ps time scale, see Figure S10. Hence, irrespective of system preparation and energy function used, isomerization from AA to VA is not found in the present simulations on the aggregate, multiple 100 ns simulations when excitation energies consistent with actinic photons are used.

Next, 10'000 *ZPE* trajectories were run for an excitation energy of 127.6 kcal/mol, as had been done in earlier computational work for AA decomposition into CH<sub>4</sub>+CO.<sup>22</sup> The error between two independently trained NNs (see Figure S2) for a typical trajectory is 0.047 kcal/mol with a standard deviation of 0.074 kcal/mol. This indicates that the NN used in the MD simulation is robust. It is worthwhile to note that at an earlier stage of the NN with a total (i.e. training, validation, and test) of 411'204 structures none of the trajectories run at an excitation energy of 127.6 kcal/mol fulfilled such a tight statistical criterion. Hence, an additional 21'195 structures was specifically added in the high-energy part of the reference data set. Without this, the present quality of the simulations could not have been achieved.

Secondly, the trajectories were categorized based on the type of reactions that occur. Out of the 10'000 runs, 9344 trajectories are unreactive – i.e. remain in the AA structure, as was found for the lower excitation energy considered above – 26 trajectories dissociate to CH<sub>4</sub>+CO, 22 react to ketene+H<sub>2</sub>, and a total of 608 isomerize to VA. Hence, by using a considerably larger excitation energy than that available from solar photons the process of interest – isomerization from AA to VA – is observed on the  $\sim 100$  ps time scale for 6 % of the trajectories. The reaction times, defined as the time difference between the start of

the trajectory and reaching an OH-separation of  $< 1 \text{ \AA}$  for the first time, are summarized in Figure S11. The reaction time distribution is flat and includes everything from prompt isomerization (few ps) to exhausting the total simulation time (50 ps).

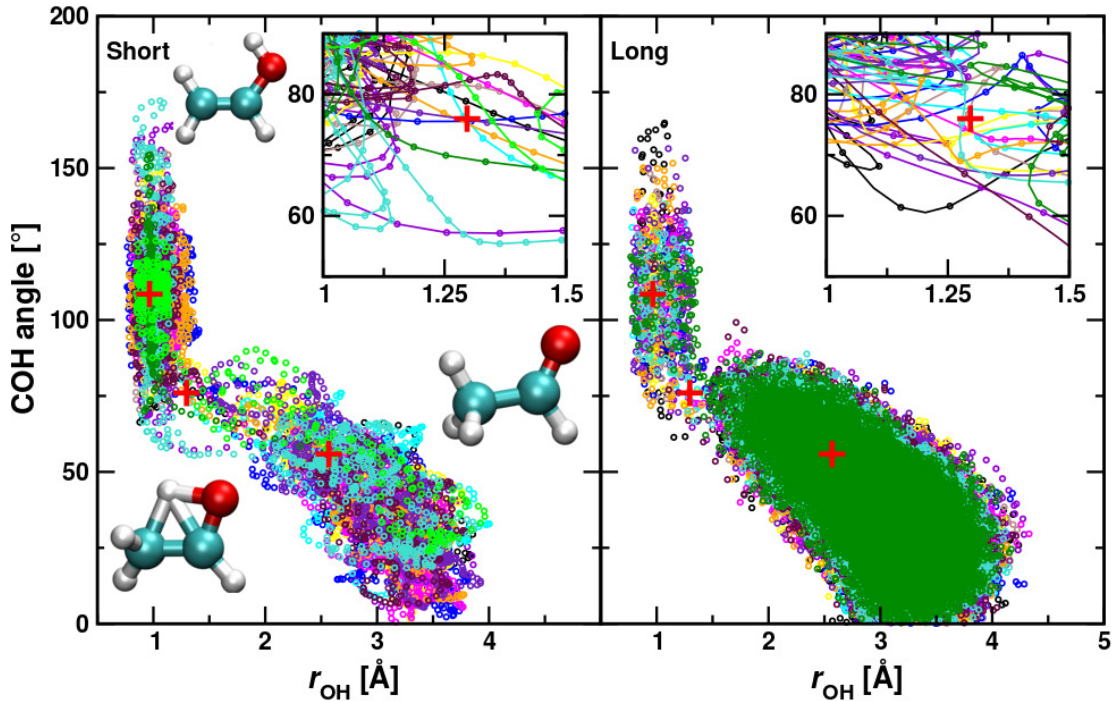


Figure 8: Projection of the reaction path from AA to VA in terms of the O–H bond length  $r_{\text{OH}}$  and COH bond angle for the trajectories with the 13 shortest and longest reaction times. Trajectories with short reaction times are shown up to 200 fs after the tautomerization. The optimized structures for AA, for VA and the TS are marked with a cross, and illustrated with the corresponding structures in the left panel.

The isomerization dynamics from AA to VA is further analyzed by considering the reaction path as a function of the OH distance and the COH angle, see Figure 8, which are two of the main coordinates involved in the process. Here, the AA structure is in the lower right-hand corner whereas that of VA is in the upper left hand corner. For short reaction times (left panel in Figure 8) the AA well is scarcely sampled whereas for trajectories with long

reaction times (right panel), exhibiting partial IVR, this is not the case. In this projection, TS1 is located in (or very close to) the region covered by the VA well. Therefore, the two coordinates chosen do not best separate reactants from products, in particular with respect to the  $r_{\text{OH}}$  coordinate. The distribution of the reactive trajectories in the region around the TS has a comparable width along the COH coordinate (see insets) although short-lived trajectories (short reaction times) sample angles down to  $55^\circ$  compared to  $60^\circ$  for longer-lived trajectories. The most apparent difference is that the short-lived trajectories cross the TS in a direct manner whereas the long-lived trajectories also show recrossings (e.g. green) before reaching the VA well. This is consistent with a ballistic mechanism for the short-lived and a structurally more heterogeneous dynamics for long-lived trajectories. As a consequence, TST-based approaches will have difficulties to correctly capture the reaction rate.

Next, the trajectories are evaluated after tautomerization has occurred. Out of 608 trajectories that tautomerize to VA, 31 re-isomerized to AA which are unlikely to proceed further to FA (i.e. cross again from AA to VA) but a thorough assessment of this is outside the scope of this work and would require considerably more and longer sampling. Furthermore, it is found that  $\sim 50\%$  of the re-isomerizing trajectories (VA $\rightarrow$ AA) access regions in configurational space poorly covered by the reference *ab initio* calculations which is reflected in occasional breaking of the C-O bond.

As soon as the system has isomerized to VA the quality of the dynamics deteriorates. This is illustrated by considering a trajectory which isomerizes (AA $\rightarrow$ VA) and then samples the VA well extensively. Visual inspection of the trajectory reveals that the OH-group temporarily dissociates but eventually rebinds to the carbon atom again. This trajectory is evaluated with two independently trained NNs and the energy predictions are compared in Figure S2. The deviation between the two NNs shows one large spike when the OH moiety dissociates. Except for this, only modest differences between the two NNs are found. However, for a

comprehensive description of the dynamics in the VA-well, additional structures would be required and the NN would have to be retrained. As this part of the dynamics is not of direct interest in the present work this was, however, not done.

## 4 Discussion and Conclusion

Using an NN trained on a large number of reference data provides an accurate, fully-dimensional and reactive PES describing AA, VA, and the dissociation to  $\text{CH}_4 + \text{H}_2$  and  $\text{H}_2 + \text{H}_2\text{C}_2\text{O}$ , see Figure 2. The PES is suitable to run reactive MD simulations and to analyze several reaction pathways. However, when running simulations with sufficiently high excitation energies to induce isomerization between AA and VA, validation of the sampled structures and energies is mandatory. In generating the NN-based PES it was found that when training on a slightly smaller data set (containing a total of 411'204 structures) the NN was not suitable for robust simulations of the AA $\rightarrow$ VA isomerization at 127.6 kcal/mol and additional reference calculations had to be included to cover the high-lying regions of the PES. Histograms showing different bond lengths for the full data set and the difference between this and the smaller data set are provided in Figures S12 to 19.

The accuracy of the fitted PES can also be discussed by considering MAEs and RMSEs in specific energy intervals relevant to the processes of interest in the present work, see Table 2. For energies below the isomerization barrier to VA (68 kcal/mol) the MAE and RMSE are 0.0081 kcal/mol and 0.0131 kcal/mol, respectively. This remains similar for energies up to the energy available in the solar spectrum ( $\sim 93.6$  kcal/mol) where the MAE is 0.0071 kcal/mol and the RMSE is 0.0145 kcal/mol. For energies corresponding to the highest excitation energy used in the simulations (127.6 kcal/mol) the MAE and the RMSE increase slightly to 0.0132 kcal/mol and 0.0307 kcal/mol, respectively. Finally, for energies

larger than 127.6 kcal/mol, a MAE of 0.1226 kcal/mol and an RMSE of 2.0728 kcal/mol are found. A system for which such data has been published is  $\text{N}_2+\text{N}_2$  for which typical RMSEs of a parametrized fit are 1.8 kcal/mol (for energies up to 100 kcal/mol) and 4.1 kcal/mol (for energies up to 228 kcal/mol), respectively.<sup>51</sup>

**Table 2: Errors (in kcal/mol) of the fitted PES with respect to the *ab initio* MP2/aug-cc-pVTZ calculations for different energy ranges. The structures of the test set are evaluated and the energy of the optimized AA structure serves as the zero of energy.**

$E$ [kcal/mol]	#	MAE( $E$ )	RMSE( $E$ )
$E < 30$	5550	0.0045	0.0067
$30 < E < 68$	5719	0.0081	0.0131
$68 < E < 93.6$	4297	0.0071	0.0145
$93.6 < E < 127.6$	2857	0.0132	0.0307
$E > 127.6$	8976	0.1226	2.0728
total	27399	0.0453	1.1865

Starting trajectories from the optimized AA structure at 93.6 kcal/mol above the minimum energy structure of AA does not lead to VA. For this, an aggregate of 0.5  $\mu\text{s}$  of reactive MD simulations was run and analyzed. It is, therefore, concluded that nonequilibrium preparation of AA through absorption of an actinic photon  $\lambda = 300$  to 330 nm (86.6 to 95.3 kcal/mol) isomerization to VA on the sub- $\mu\text{s}$  time scale is unlikely to occur.

The present PES can also be used to study decomposition into  $\text{CH}_4+\text{CO}$  and  $\text{H}_2+\text{H}_2\text{CCO}$  which is, however, outside the scope of the present work. Previous efforts included simulations for the  $\text{AA} \rightarrow \text{CH}_3+\text{HCO}$  and the  $\text{AA} \rightarrow \text{CH}_4+\text{CO}$  dissociation from *ab initio* MD simulations,<sup>52–54</sup> for the  $\text{AA} \rightarrow \text{H}_2\text{CO}+\text{H}_2$  dissociation on a reaction path potential<sup>55</sup> and QCT simulations on a global *ab initio*-based PES fitted using permutationally invariant polynomials (PIPs).<sup>23</sup> Additionally, the roaming dynamics in the dissociation of acetaldehyde was examined using a reduced dimensionality trajectory approach<sup>56</sup> and using a full-dimensional PES fit with PIPs.<sup>22</sup>

Because the *EX* trajectories yielded no reactive events and it was found that IVR is an impeding factor to reactivity and isomerization, RRKM (statistical rate) calculations were also carried out. Rate constants  $k(E)$  are determined with the MultiWell 2016 suite of programs.<sup>57</sup> Key parameters (harmonic frequencies, energies of the critical points, see Tables S1 and S2) are obtained from the NN (trained at MP2/aug-cc-pVTZ) and the rates were computed for two different total energies, 93.6 and 127.6 kcal/mol, corresponding to the two types of MD simulations carried out. The isomerization reactions  $AA \leftrightarrow VA$  occur on the ns time scale, see Table 3 whereas the dissociation reactions (to  $CH_4 + CO$  and  $H_2 + \text{ketene}$ ) with energies of 93.6 kcal/mol are predicted to occur on the  $\mu s$  time scale. With an energy of 127.6 kcal/mol both decomposition reaction rates are on the ns time scale.

Such rates are consistent with earlier work. At the B3LYP level of theory the RRKM rate for photodissociation<sup>58</sup> of AA to  $CH_4 + CO$  at 121.76 kcal/mol (i.e. 5.28 eV)  $k(E) = 4.47 \times 10^9$  compared with  $k(E) = 1.715 \times 10^9$  from the present calculations using the NN-trained PES. Similar work considering statistical rates has been done on AA. It includes the dissociation of AA following excitation into  $S_1$ <sup>59</sup> or the FA-assisted tautomerization of AA.<sup>25</sup>

**Table 3: Rates [ $s^{-1}$ ] for the possible AA reactions at two different total energies used in the MD simulations.**

$k(E)$ [ $s^{-1}$ ]	93.6 kcal/mol	127.6 kcal/mol
$VA \rightarrow AA$	$7.209 \times 10^8$	$2.073 \times 10^{10}$
$AA \rightarrow VA$	$1.569 \times 10^8$	$5.865 \times 10^9$
$AA \rightarrow H_2 + H_2CCO$	$2.612 \times 10^6$	$1.098 \times 10^9$
$AA \rightarrow CH_4 + CO$	$1.699 \times 10^6$	$3.756 \times 10^9$

On the other hand, running simulations including zero-point vibrational energy at a total energy of 127 kcal/mol readily leads to isomerization on the 100 ps time scale (608 events in 500 ns). The fact that for the dynamics in the VA well the NN may have deficiencies does not affect this conclusion because up to TS1, separating AA from VA, the quality of the NN

is very good.

The flat reaction time distribution for isomerization between AA and VA differs from reaction time distributions for water elimination from  $\text{H}_2\text{SO}_4$  after vibrational excitation of an overtone OH-stretch vibration<sup>8,60</sup> where they followed a Poissonian distributions. Since in the present case the initial preparation is thermal and not mode specific and IVR is very rapid it is conceivable that the distribution of reaction times is flat. In other words, after relaxing into the AA well, the energy (here 127.6 kcal/mol) is either used to isomerize in a ballistic manner or isomerization to VA occurs after partial relaxation on longer time scales. For the smaller excitation energy (93.6 kcal/mol) only relaxation into AA was observed on the time scale of the simulations (aggregate of 500 ns).

Whether or not isomerization of AA to VA in the atmosphere is relevant for FA generation depends, therefore, on the competition between IVR and collisional de-excitation. Under upper stratospheric-lower mesospheric conditions the deactivation of excited molecules due to collisions with other molecules are relevant. For  $\text{H}_2\text{SO}_4$  at typical polar (75°S) conditions in the stratopause (at a height of 50 km with pressure  $p \sim 70$  Pa and temperature  $T \sim 280$  K) quenching occurs on the 130 ns timescale (inverse of the collision frequency  $Z$ ,  $\tau_{\text{quench}} = (Z[\text{M}])^{-1}$ ).<sup>8</sup> Given their similar mass and size,  $\text{H}_2\text{SO}_4$  and AA are expected to behave similarly and it is expected that this time scale is also representative for AA. If after photoexcitation and returning to the ground state AA has not isomerized (to VA) or decayed (to products) within  $\sim 100$  ns, it is likely that de-excitation occurs through collisions. Further chemical processing, including isomerization and decomposition, is not possible then. Hence, formation of FA following electronic excitation with actinic photons of AA and subsequent ground state relaxation and isomerization to VA appears unlikely to occur.

## 5 Acknowledgments

This work was supported by the Swiss National Science Foundation through grants 200021-117810, 200020-188724, the NCCR MUST, and the University of Basel. OTU acknowledges funding from the Swiss National Science Foundation (Grant No. P2BSP2\_188147).

## References

- (1) Vereecken, L.; Aumont, B.; Barnes, I.; Bozzelli, J.; Goldman, M.; Green, W.; Madronich, S.; McGillen, M.; Mellouki, A.; Orlando, J. et al. Perspective on mechanism development and structure-activity relationships for gas-phase atmospheric chemistry. *Int. J. Chem. Kinet.* **2018**, *50*, 435–469.
- (2) Shaw, M. F.; Sztáray, B.; Whalley, L. K.; Heard, D. E.; Millet, D. B.; Jordan, M. J.; Osborn, D. L.; Kable, S. H. Photo-tautomerization of acetaldehyde as a photochemical source of formic acid in the troposphere. *Nat. Commun.* **2018**, *9*, 1–7.
- (3) Archibald, A. T.; McGillen, M. R.; Taatjes, C. A.; Percival, C. J.; Shallcross, D. E. Atmospheric transformation of enols: A potential secondary source of carboxylic acids in the urban troposphere. *Geophys. Res. Lett.* **2007**, *34*.
- (4) Andrews, D. U.; Heazlewood, B. R.; Maccarone, A. T.; Conroy, T.; Payne, R. J.; Jordan, M. J. T.; Kable, S. H. Photo-Tautomerization of Acetaldehyde to Vinyl Alcohol: A Potential Route to Tropospheric Acids. *Science* **2012**, *337*, 1203–1206.
- (5) Clubb, A. E.; Jordan, M. J. T.; Kable, S. H.; Osborn, D. L. Phototautomerization of Acetaldehyde to Vinyl Alcohol: A Primary Process in UV-Irradiated Acetaldehyde from 295 to 335 nm. *J. Phys. Chem. Lett.* **2012**, *3*, 3522–3526.
- (6) Miller, Y.; Gerber, R. B. Dynamics of Vibrational Overtone Excitations of H<sub>2</sub>SO<sub>4</sub>,



- H<sub>2</sub>SO<sub>4</sub>-H<sub>2</sub>O: Hydrogen-Hopping and Photodissociation Processes. *J. Am. Chem. Soc.* **2006**, *128*, 9594 – 9595.
- (7) Nagy, T.; Yosa Reyes, J.; Meuwly, M. Multisurface Adiabatic Reactive Molecular Dynamics. *J. Chem. Theory. Comput.* **2014**, *10*, 1366–1375.
  - (8) Yosa Reyes, J.; Nagy, T.; Meuwly, M. Competitive Reaction Pathways in Vibrationally Induced Photodissociation of H<sub>2</sub>SO<sub>4</sub>. *Phys. Chem. Chem. Phys.* **2014**, *16*, 18533–18544.
  - (9) Reyes, J. Y.; Brickel, S.; Unke, O. T.; Nagy, T.; Meuwly, M. HSO<sub>3</sub>Cl: A Prototype Molecule for Studying OH-stretching Overtone Induced Photodissociation. *Phys. Chem. Chem. Phys.* **2016**, *18*, 6780–6788.
  - (10) Vaida, V.; Kjaergaard, H. G.; Hintze, P. E.; Donaldson, D. J. Photolysis of sulfuric acid vapor by visible solar radiation. *Science* **2003**, *299*, 1566–1568.
  - (11) Zhong, J.; Li, H.; Kumar, M.; Liu, J.; Liu, L.; Zhang, X.; Zeng, X. C.; Francisco, J. S. Mechanistic Insight into the Reaction of Organic Acids with SO<sub>3</sub> at the Air-Water Interface. *Angew. Chem. Int. Ed.* **2019**, *58*, 8351–8355.
  - (12) Farah, K.; Mueller-Plathe, F.; Boehm, M. C. Classical Reactive Molecular Dynamics Implementations: State of the Art. *Chem. Phys. Chem.* **2012**, *13*, 1127–1151.
  - (13) Meuwly, M. Reactive molecular dynamics: From small molecules to proteins. *Wiley Interdiscip. Rev. Comput. Mol. Sci.* **2019**, *9*, e1386.
  - (14) McCulloch, W. S.; Pitts, W. A logical calculus of the ideas immanent in nervous activity. *Bull. Math. Sci.* **1943**, *5*, 115–133.
  - (15) Rosenblatt, F. The perceptron: A probabilistic model for information storage and organization in the brain. *Psychol. Rev.* **1958**, *65*, 386–408.
  - (16) Behler, J. Neural network potential-energy surfaces in chemistry: a tool for large-scale simulations. *Phys. Chem. Chem. Phys.* **2011**, *13*, 17930–17955.

- (17) Schalkoff, R. J. *Artificial neural networks*; McGraw-Hill New York, 1997; Vol. 1.
- (18) Hornik, K.; Stinchcombe, M.; White, H. Multilayer feedforward networks are universal approximators. *Neural Netw.* **1989**, *2*, 359–366.
- (19) Finlayson-Pitts, B. J.; Pitts Jr, J. N. *Chemistry of the upper and lower atmosphere: theory, experiments, and applications*; Elsevier, 1999.
- (20) Millet, D. B.; Baasandorj, M.; Farmer, D. K.; Thornton, J. A.; Baumann, K.; Brophy, P.; Chaliyakunnel, S.; de Gouw, J. A.; Graus, M.; Hu, L. et al. A large and ubiquitous source of atmospheric formic acid. *Atmos. Chem. Phys* **2015**, *15*, 6283–6304.
- (21) So, S.; Wille, U.; da Silva, G. Atmospheric Chemistry of Enols: A Theoretical Study of the Vinyl Alcohol + OH + O<sub>2</sub> Reaction Mechanism. *Environ. Sci. Technol* **2014**, *48*, 6694–6701.
- (22) Shepler, B. C.; Braams, B. J.; Bowman, J. M. Quasiclassical trajectory calculations of acetaldehyde dissociation on a global potential energy surface indicate significant non-transition state dynamics. *J. Phys. Chem. A* **2007**, *111*, 8282–8285.
- (23) Han, Y.-C.; Shepler, B. C.; Bowman, J. M. Quasiclassical Trajectory Calculations of the Dissociation Dynamics of CH<sub>3</sub>CHO at High Energy Yield Many Products. *J. Phys. Chem. Lett.* **2011**, *2*, 1715–1719.
- (24) Braams, B. J.; Bowman, J. M. Permutationally Invariant Potential Energy Surfaces in High Dimensionality. *Int. Rev. Phys. Chem.* **2009**, *28*, 577–606.
- (25) Peeters, J.; Nguyen, V. S.; Muller, J.-F. Atmospheric Vinyl Alcohol to Acetaldehyde Tautomerization Revisited. *J. Phys. Chem. Lett.* **2015**, *6*, 4005–4011.
- (26) Unke, O. T.; Brickel, S.; Meuwly, M. Sampling reactive regions in phase space by following the minimum dynamic path. *J. Chem. Phys.* **2019**, *150*, 074107.

- (27) Larsen, A. H.; Mortensen, J. J.; Blomqvist, J.; Castelli, I. E.; Christensen, R.; Dułak, M.; Friis, J.; Groves, M. N.; Hammer, B.; Hargus, C. et al. The atomic simulation environment – a Python library for working with atoms. *J. Phys. Condens. Matter.* **2017**, *29*, 273002.
- (28) Unke, O. T.; Meuwly, M. PhysNet: a neural network for predicting energies, forces, dipole moments, and partial charges. *J. Chem. Theory. Comput.* **2019**, *15*, 3678–3693.
- (29) Behler, J.; Parrinello, M. Generalized neural-network representation of high-dimensional potential-energy surfaces. *Phys. Rev. Lett.* **2007**, *98*, 146401.
- (30) Unke, O. T.; Meuwly, M. A reactive, scalable, and transferable model for molecular energies from a neural network approach based on local information. *J. Chem. Phys.* **2018**, *148*, 241708.
- (31) Gilmer, J.; Schoenholz, S. S.; Riley, P. F.; Vinyals, O.; Dahl, G. E. Neural message passing for quantum chemistry. Proceedings of the 34th International Conference on Machine Learning-Volume 70. 2017; pp 1263–1272.
- (32) Grimme, S.; Antony, J.; Ehrlich, S.; Krieg, H. A consistent and accurate ab initio parametrization of density functional dispersion correction (DFT-D) for the 94 elements H-Pu. *J. Chem. Phys.* **2010**, *132*, 154104.
- (33) Grimme, S.; Ehrlich, S.; Goerigk, L. Effect of the damping function in dispersion corrected density functional theory. *J. Comput. Chem.* **2011**, *32*, 1456–1465.
- (34) Baydin, A. G.; Pearlmutter, B. A.; Radul, A. A.; Siskind, J. M. Automatic differentiation in machine learning: a survey. *J. Mach. Learn. Res.* **2018**, *18*, 1–43.
- (35) Møller, C.; Plesset, M. S. Note on an approximation treatment for many-electron systems. *Phys. Rev.* **1934**, *46*, 618.

- (36) Dunning Jr, T. H. Gaussian basis sets for use in correlated molecular calculations. I. The atoms boron through neon and hydrogen. *J. Chem. Phys.* **1989**, *90*, 1007–1023.
- (37) Werner, H.-J.; Knowles, P. J.; Knizia, G.; Manby, F. R.; Schütz, M.; Celani, P.; Györffy, W.; Kats, D.; Korona, T.; Lindh, R. et al. MOLPRO, version 2018.2, a package of ab initio programs. 2018.
- (38) Huang, B.; von Lilienfeld, O. A. The “DNA” of chemistry: Scalable quantum machine learning with ”amons”. *arXiv preprint arXiv:1707.04146* **2017**,
- (39) Stewart, J. J. Optimization of parameters for semiempirical methods V: modification of NDDO approximations and application to 70 elements. *J. Mol. Model.* **2007**, *13*, 1173–1213.
- (40) J.J.P. Stewart, S. C. C. MOPAC 2016. 2016; Colorado Springs, CO, USA.
- (41) Torrie, G. M.; Valleau, J. P. Nonphysical sampling distributions in Monte Carlo free-energy estimation: Umbrella sampling. *J. Comput. Phys.* **1977**, *23*, 187–199.
- (42) Behler, J. Perspective: Machine learning potentials for atomistic simulations. *J. Chem. Phys* **2016**, *145*, 170901.
- (43) Behler, J. Constructing high-dimensional neural network potentials: A tutorial review. *Int. J. Quantum Chem.* **2015**, *115*, 1032–1050.
- (44) Smith, J. S.; Isayev, O.; Roitberg, A. E. ANI-1: an extensible neural network potential with DFT accuracy at force field computational cost. *Chem. Sci.* **2017**, *8*, 3192–3203.
- (45) Rivero, U.; Unke, O. T.; Meuwly, M.; Willitsch, S. Reactive atomistic simulations of Diels-Alder reactions: The importance of molecular rotations. *J. Chem. Phys.* **2019**, *151*, 104301.
- (46) Verlet, L. Computer “Experiments” on Classical Fluids. I. Thermodynamical Properties of Lennard-Jones Molecules. *Phys. Rev.* **1967**, *159*, 98.

- (47) Shepler, B. C.; Braams, B. J.; Bowman, J. M. Quasiclassical trajectory calculations of acetaldehyde dissociation on a global potential energy surface indicate significant non-transition state dynamics. *J. Phys. Chem. A* **2007**, *111*, 8282–8285.
- (48) Lee, T. J.; Taylor, P. R. A diagnostic for determining the quality of single-reference electron correlation methods. *Int. J. Quantum Chem.* **1989**, *36*, 199–207.
- (49) Ma, Q.; Werner, H.-J. Explicitly correlated local coupled-cluster methods using pair natural orbitals. *Wiley Interdiscip. Rev. Comput. Mol. Sci.* **2018**, *8*, e1371.
- (50) Bannwarth, C.; Ehlert, S.; Grimme, S. GFN2-xTB – An accurate and broadly parametrized self-consistent tight-binding quantum chemical method with multipole electrostatics and density-dependent dispersion contributions. *J. Chem. Theory Comput.* **2019**, *15*, 1652–1671.
- (51) Paukku, Y.; Yang, K. R.; Varga, Z.; Truhlar, D. G. Global ab initio ground-state potential energy surface of N<sub>4</sub>. *J. Chem. Phys.* **2013**, *139*, 044309.
- (52) Kurosaki, Y.; Yokoyama, K. Photodissociation of acetaldehyde, CH<sub>3</sub>CHO → CH<sub>3</sub> + HCO: direct ab initio molecular dynamics study. *Chem. Phys. Lett.* **2003**, *371*, 568–575.
- (53) Kurosaki, Y.; Yokoyama, K. Photodissociation of acetaldehyde, CH<sub>3</sub>CHO → CH<sub>4</sub> + CO: direct ab initio dynamics study. *J. Phys. Chem. A* **2002**, *106*, 11415–11421.
- (54) Kurosaki, Y. Photodissociation of acetaldehyde, CH<sub>3</sub>CHO → CH<sub>4</sub> + CO: II. Direct ab initio molecular dynamics study. *Chem. Phys. Lett.* **2006**, *421*, 549–553.
- (55) Harrison, A. W.; Kharazmi, A.; Shaw, M. F.; Quinn, M. S.; Lee, K. K.; Nauta, K.; Rowell, K. N.; Jordan, M. J.; Kable, S. H. Dynamics and quantum yields of H<sub>2</sub> + CH<sub>2</sub>CO as a primary photolysis channel in CH<sub>3</sub>CHO. *Phys. Chem. Chem. Phys.* **2019**, *21*, 14284–14295.

- (56) Harding, L. B.; Georgievskii, Y.; Klippenstein, S. J. Roaming radical kinetics in the decomposition of acetaldehyde. *The Journal of Physical Chemistry A* **2010**, *114*, 765–777.
- (57) Barker, J. R. Multiple-Well, multiple-path unimolecular reaction systems. I. MultiWell computer program suite. *Int. J. Chem. Kinet.* **2001**, *33*, 232–245.
- (58) Gherman, B. F.; Friesner, R. A.; Wong, T.-H.; Min, Z.; Bersohn, R. Photodissociation of acetaldehyde: the  $\text{CH}_4 + \text{CO}$  channel. *J. Chem. Phys.* **2001**, *114*, 6128–6133.
- (59) Tachikawa, H.; Ohta, N. Photodissociation mechanism of acetaldehyde. RRK and RRKM study. *Chem. Phys. Lett.* **1994**, *224*, 465–469.
- (60) Yosa, J.; Meuwly, M. Vibrationally Induced Dissociation of Sulfuric Acid ( $\text{H}_2\text{SO}_4$ ). *J. Phys. Chem. A* **2011**, *115*, 14350–14360.

# Supporting Information: Isomerization and Decomposition Reactions of Acetaldehyde Relevant to Atmospheric Processes from Dynamics Simulations on Neural Network-Based Potential Energy Surfaces

Silvan Käser,<sup>†</sup> Oliver T. Unke,<sup>‡</sup> and Markus Meuwly<sup>\*,†</sup>

<sup>†</sup>*Department of Chemistry, University of Basel, Klingelbergstrasse 80 , CH-4056 Basel,  
Switzerland.*

<sup>‡</sup>*Department of Chemistry, University of Basel, Klingelbergstrasse 80, CH-4056 Basel,  
Switzerland*

*Present Address: Machine Learning Group, TU Berlin, Marchstr. 23, 10587 Berlin,  
Germany*

E-mail: m.meuwly@unibas.ch

# 1 Reference Structure Set

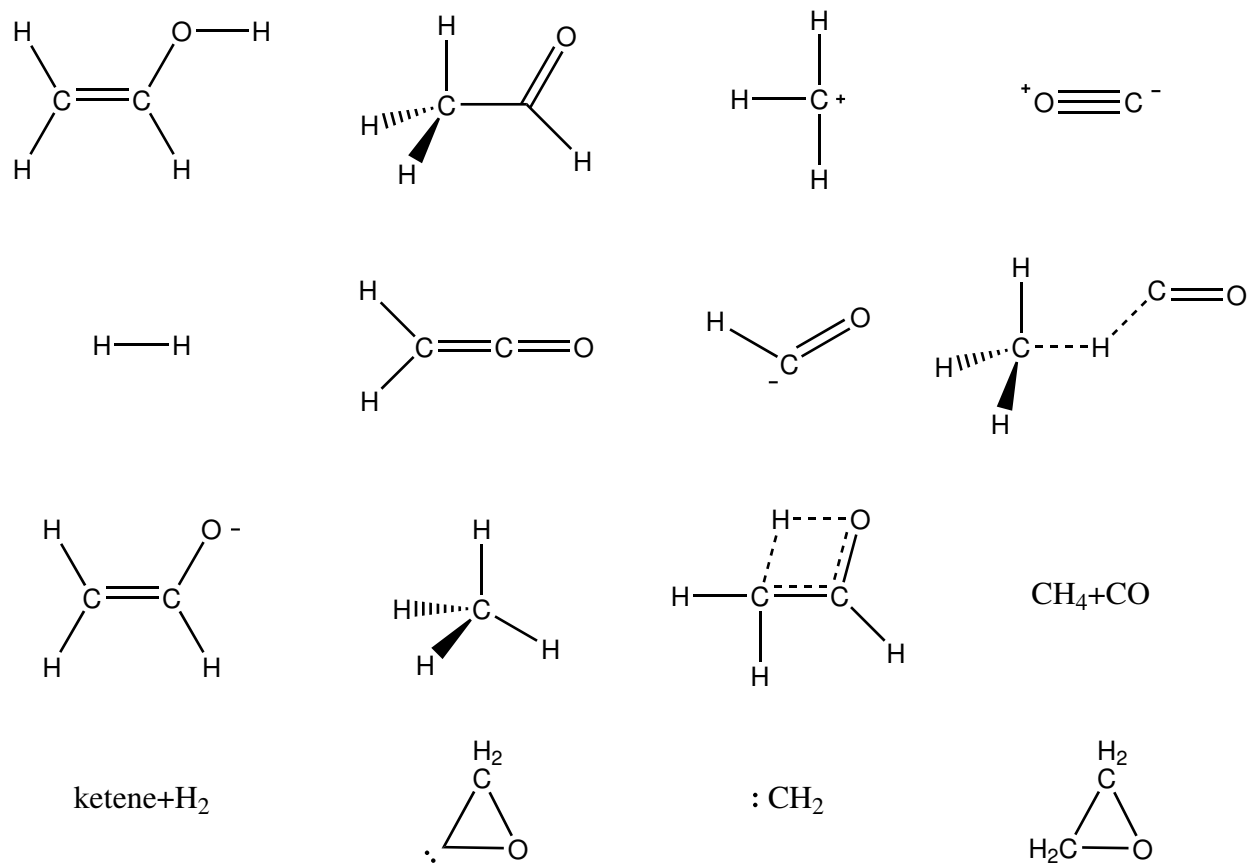


Figure S1: Schematic representation of all molecules and compounds (“amons”) used in NN training for the acetaldehyde PES.



## 2 NN Energy Comparison

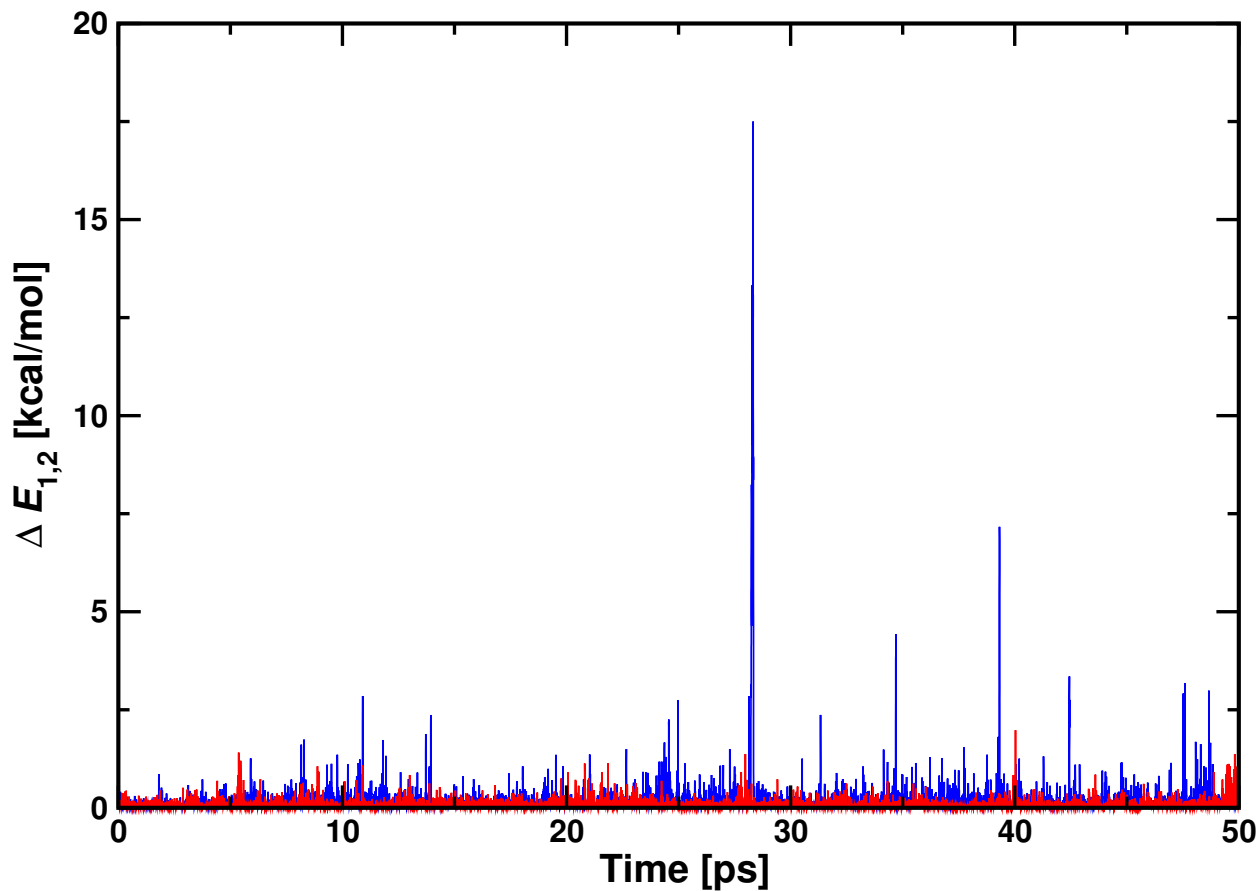


Figure S2: Energy deviation between the two independently trained NNs for a random unreactive trajectory (red) and a random reactive trajectory (blue, containing a tautomerization to VA) run at 127.6 kcal/mol. The unreactive trajectory has a mean of 0.047 kcal/mol and a standard deviation of 0.074 kcal/mol, whereas the reactive trajectory has a mean of 0.108 kcal/mol and a standard deviation of 0.476 kcal/mol. The large spike in the blue curve marks where the OH moiety dissociates and illustrates that the NN is not robust.

### 3 Systematic Outliers

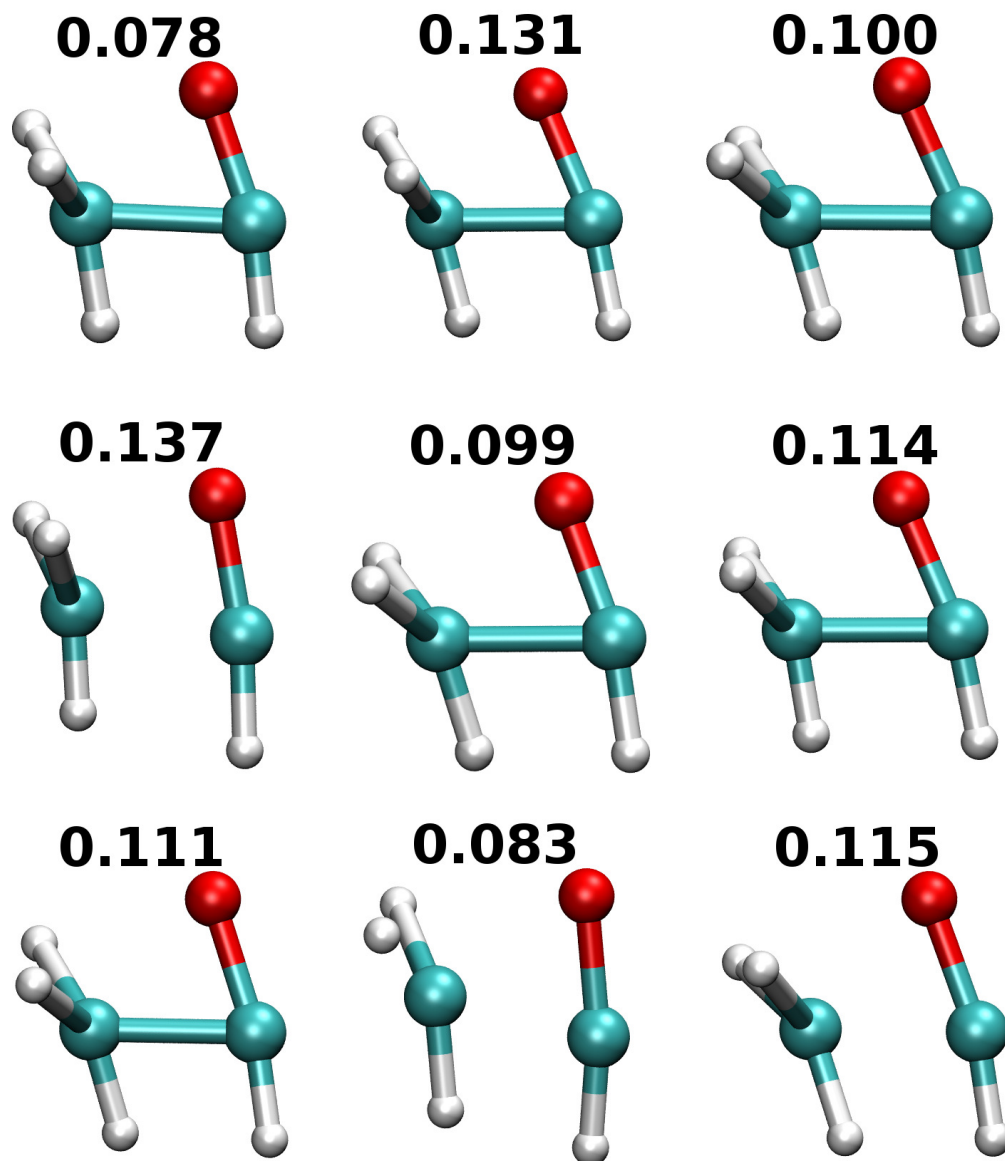


Figure S3: Illustration of structures from the test set showing a statistical error in the energy prediction of the NN. Moreover, the  $T_1$  value is shown and bonds are illustrated up to 2.7 Å.

## 4 Minimum Dynamic Path

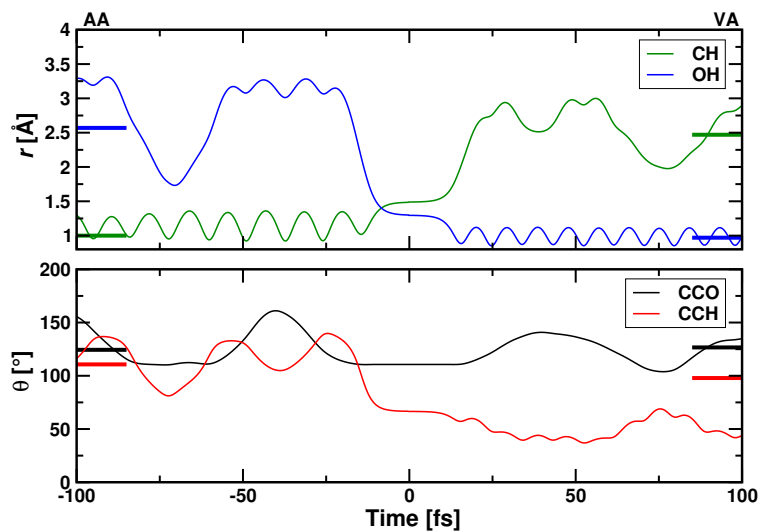


Figure S4: Evolution of different geometric properties during the MDP of the tautomerization reaction. The bars mark the equilibrium values for AA (left) and VA (right).

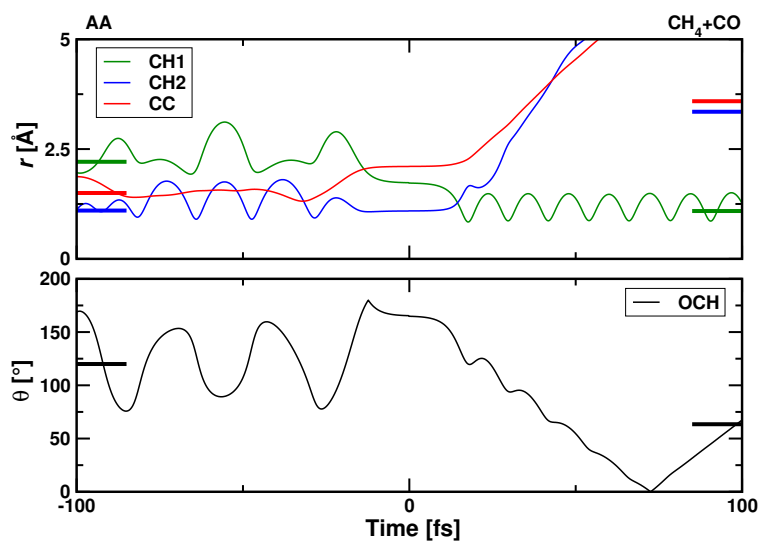


Figure S5: Evolution of different geometric properties during the MDP of the dissociation reaction forming CO and CH<sub>4</sub>. The bars mark the equilibrium values for AA (left) and the CH<sub>4</sub>+CO dissociation product.

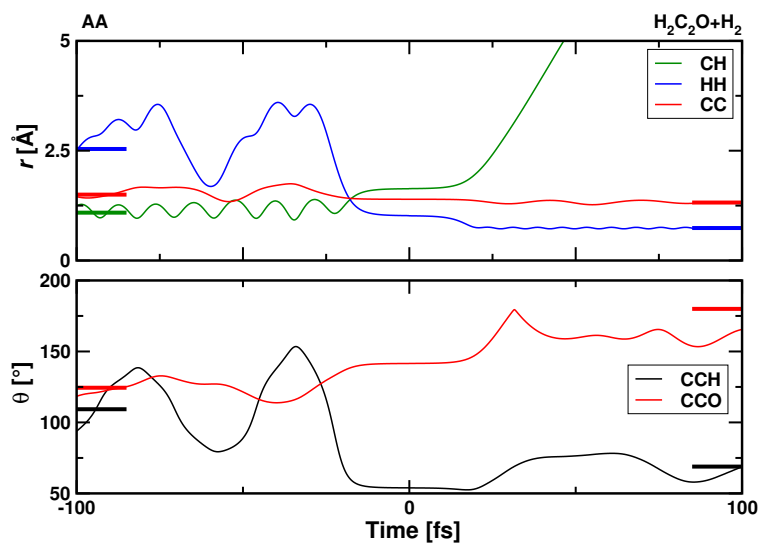


Figure S6: Evolution of different geometric properties during the MDP of the dissociation reaction forming H<sub>2</sub>CCO and H<sub>2</sub>. The bars mark the equilibrium values for AA (left) and the H<sub>2</sub>CCO and H<sub>2</sub> dissociation product.

## 5 Minimum Energy Path

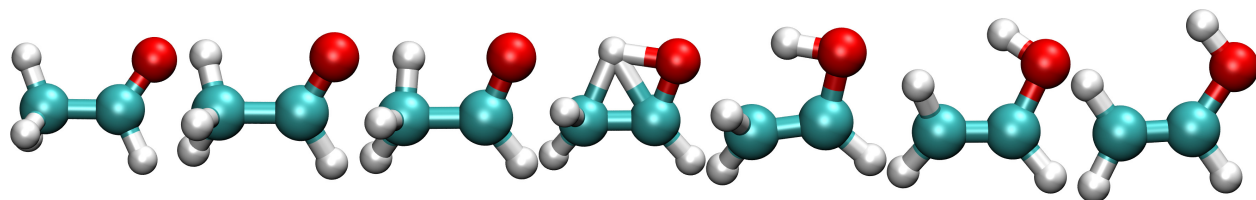


Figure S7: MEP for the tautomerization reaction.

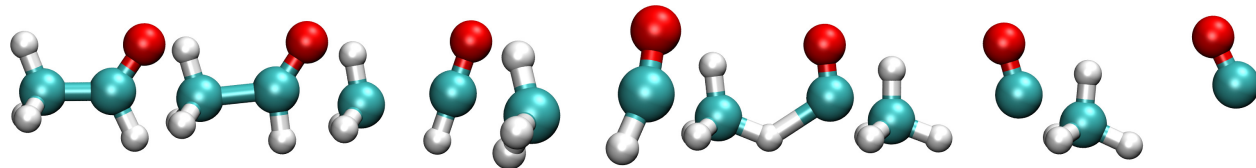


Figure S8: MEP for the dissociation to  $\text{CH}_4$  and  $\text{CO}$ .

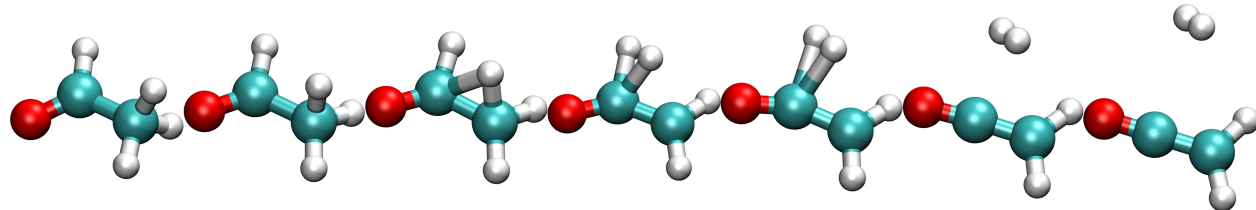


Figure S9: MEP for the dissociation to  $\text{H}_2$  and  $\text{H}_2\text{CCO}$ .

## 6 EX Trajectories

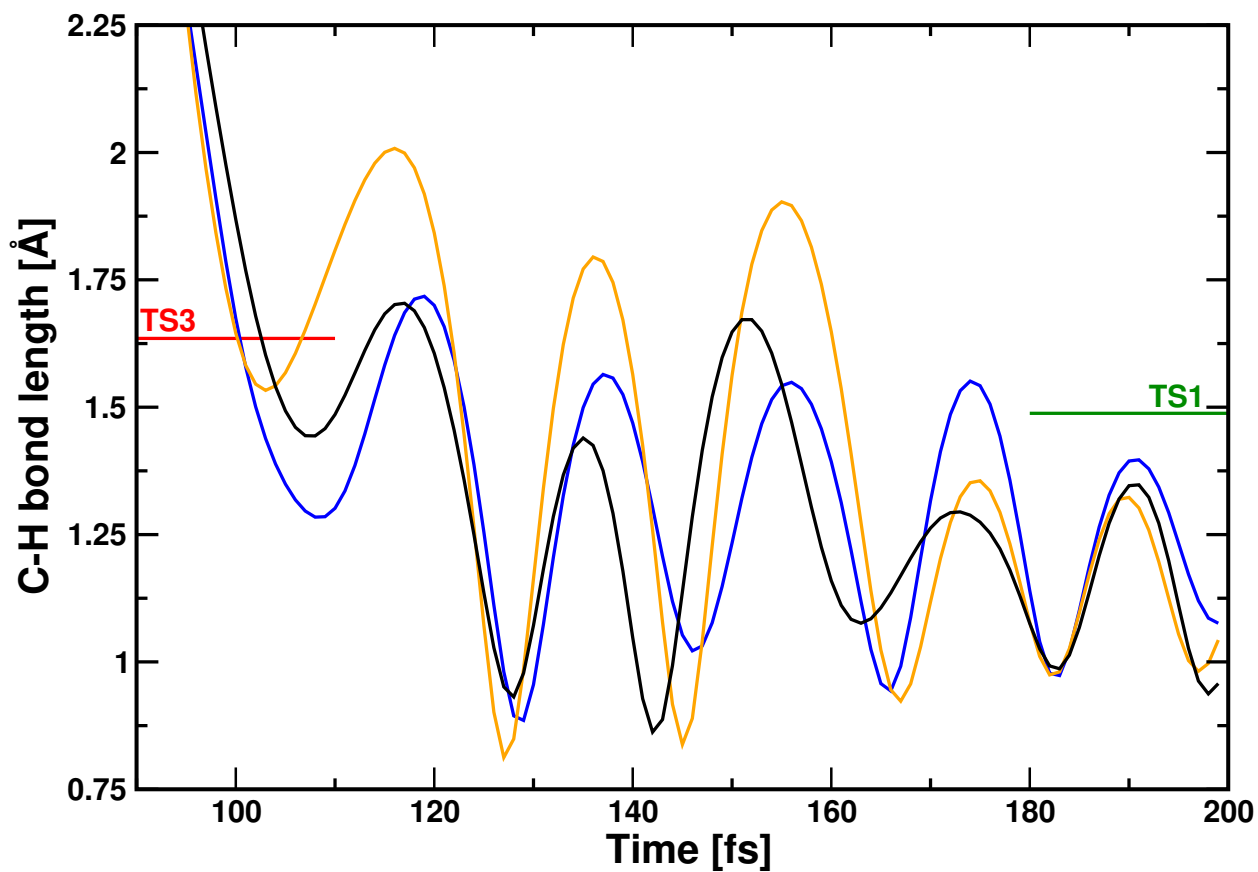


Figure S10: The progression in time for the C–H stretch motion is shown for three trajectories calculated using the GFN2-xTB method. A rapid decrease of the magnitude in C–H stretching is visible after two or three oscillations. The red line indicates the C–H bond length of TS3 (see Fig. 3).

## 7 ZPE Trajectories

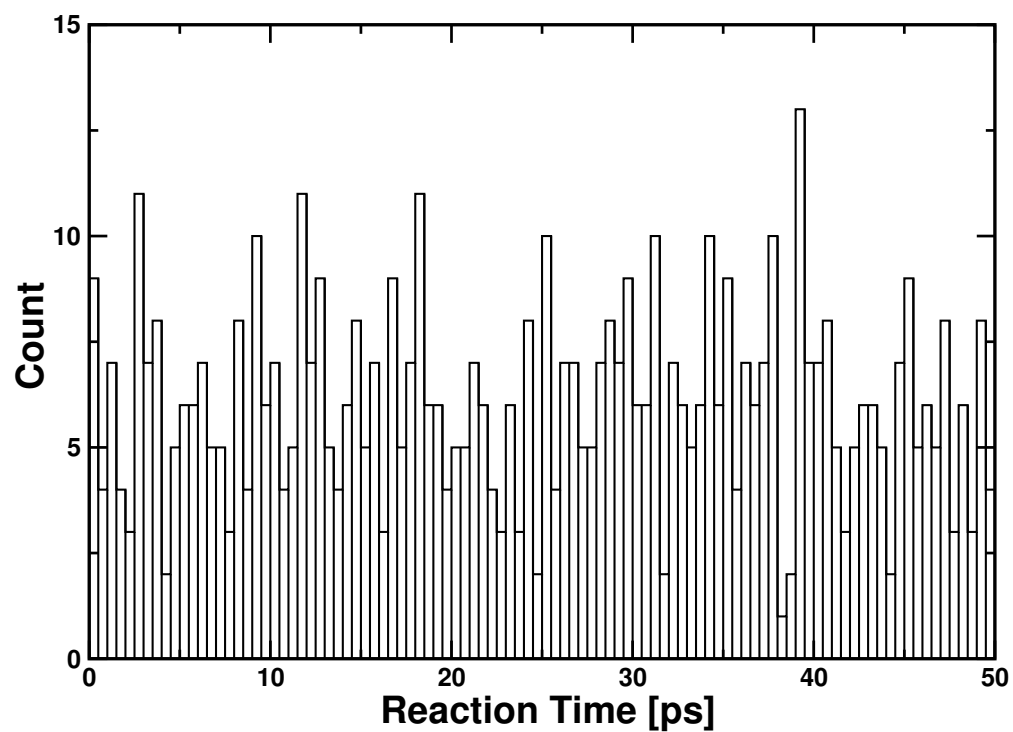


Figure S11: Histogram representing the simulation time before the tautomerization from AA to VA for a total of 608 tautomerizations.

## 8 Bond Length Distributions

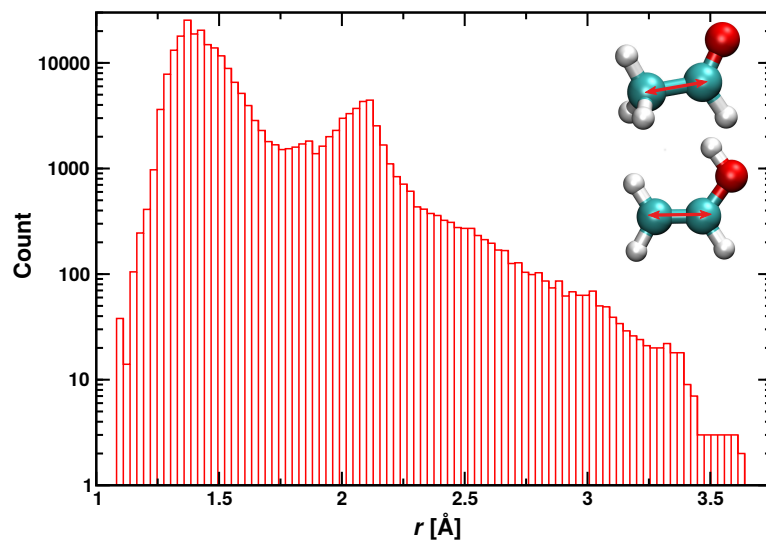


Figure S12: Histogram of the CC bond lengths (red arrows) for molecules VA (bottom) and AA (top) molecules.



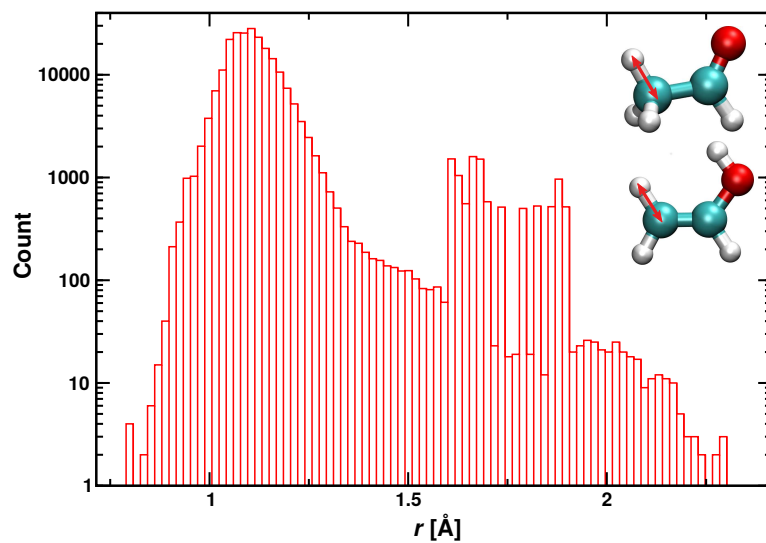


Figure S13: Histogram of one methyl/methylene CH bond (red arrows) lengths for molecules VA (bottom) and AA (top) molecules.

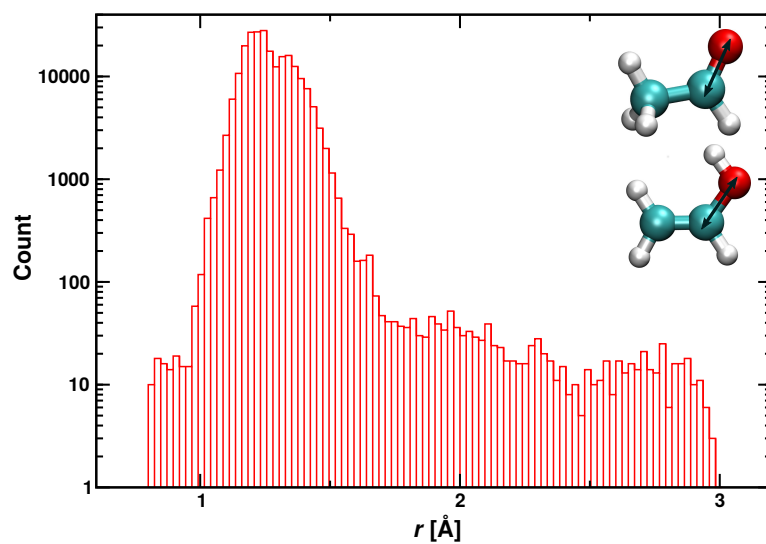


Figure S14: Histogram of the CO bond lengths (black arrows) for molecules VA (bottom) and AA (top) molecules.

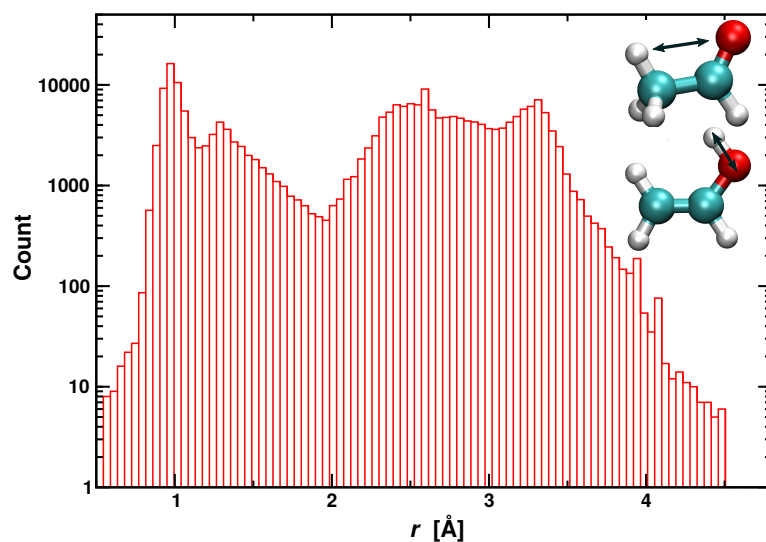


Figure S15: Histogram of the OH bond lengths (black arrows) for molecules VA (bottom) and AA (top) molecules.

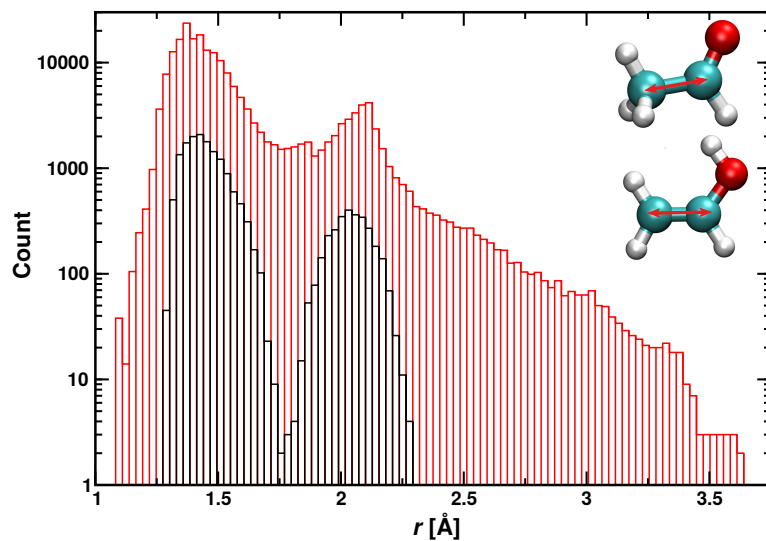


Figure S16: Histogram of the CC bond lengths (red arrows) for molecules VA (bottom) and AA (top) molecules contained in the old data set with 411'204 structures. The black histogram illustrates the difference to the new data set.

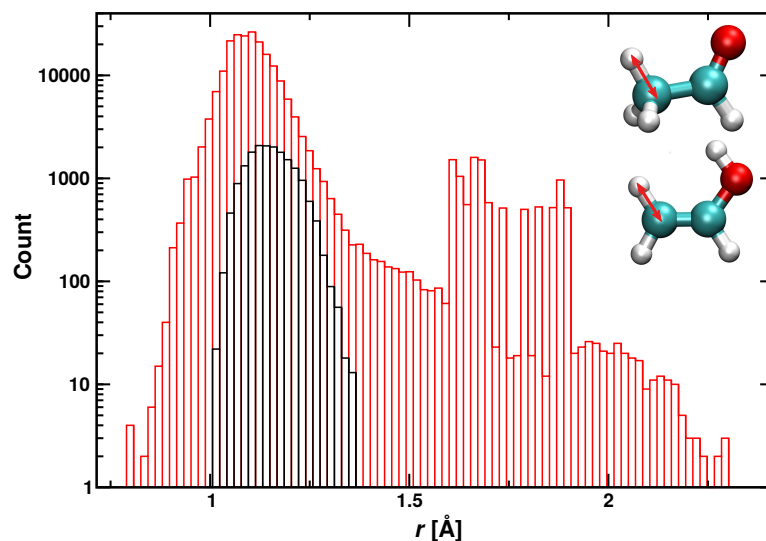


Figure S17: Histogram of one methyl/methylene CH bond (red arrows) lengths for molecules VA (bottom) and AA (top) molecules contained in the old data set with 411'204 structures. The black histogram illustrates the difference to the new data set.

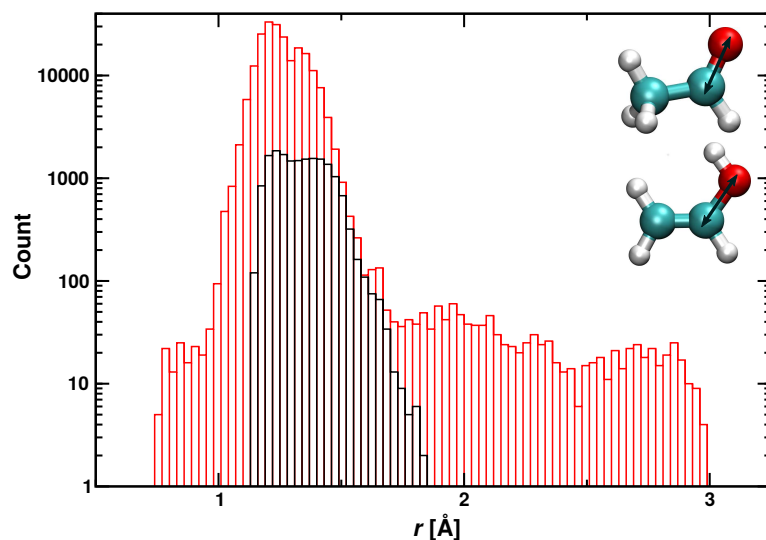


Figure S18: Histogram of the CO bond lengths (black arrows) for molecules VA (bottom) and AA (top) molecules contained in the old data set with 411'204 structures. The black histogram illustrates the difference to the new data set.

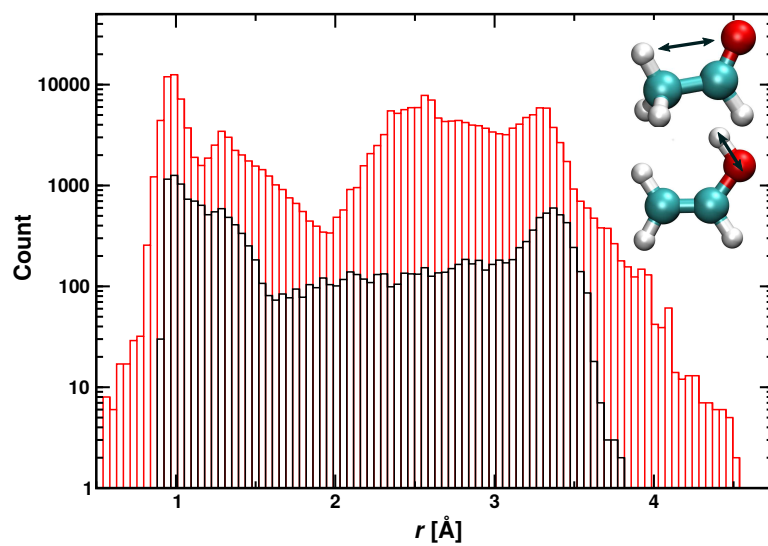


Figure S19: Histogram of the OH bond lengths (black arrows) for molecules VA (bottom) and AA (top) molecules contained in the old data set with 411'204 structures. The black histogram illustrates the difference to the new data set.

## 9 RRKM Parameters

Table S1: Energies for the optimum and TS structures used in the RRKM calculation based on the NN trained at the MP2/aug-cc-pVTZ level of theory. For the RRKM calculation, the energy barrier is ZPE corrected.

Molecule	$E$ [kcal/mol]	$E_{\text{ZPE}}$ [kcal/mol]
VA	10.1	35.6
AA	0.0	35.1
CH <sub>4</sub> +CO	-2.2	
ketene+H <sub>2</sub>	33.8	
TS1	68.1	34.8
TS2	88.2	31.8
TS3	84.2	33.2

Table S2: NN-based frequencies for the optimum and TS structures used in the RRKM calculation.

VA	AA	TS1	TS2	TS3
445.8	161.4	2202.6i	1731.0i	1514.0i
484.4	506.7	595.3	132.5	484.8
714.8	779.8	637.3	312.1	571.0
823.5	905.4	783.8	489.8	684.5
958.1	1136.3	971.4	551.9	866.2
996.2	1143.8	1062.8	740.4	960.3
1118.4	1390.7	1149.4	886.8	1102.6
1323.6	1426.6	1215.9	1057.8	1185.7
1353.0	1481.6	1299.5	1442.3	1267.8
1449.1	1493.9	1469.8	1445.0	1482.9
1696.0	1763.4	1539.3	1831.4	1656.7
3190.9	2954.4	1886.0	3044.3	1882.0
3242.8	3069.5	3137.0	3179.0	2150.5
3301.2	3148.8	3168.6	3193.6	3166.4
3804.8	3200.0	3243.2	3206.9	3284.5